TU Delft COVID-app

A tool to democratize CFD simulations for SARS-CoV-2 infection risk analysis

Faleiros, David Engler; van den Bos, Wouter; Botto, Lorenzo; Scarano, Fulvio

DOI
10.1016/j.scitotenv.2022.154143

Publication date
2022

Document Version
Final published version

Published in
Science of the Total Environment

Citation (APA)
Faleiros, D. E., van den Bos, W., Botto, L., & Scarano, F. (2022). TU Delft COVID-app: A tool to democratize CFD simulations for SARS-CoV-2 infection risk analysis. *Science of the Total Environment*, *826*, Article 154143. https://doi.org/10.1016/j.scitotenv.2022.154143

Science of the Total Environment 826 (2022) 154143

Contents lists available at ScienceDirect

Science of the Total Environment

journal homepage: www.elsevier.com/locate/scitotenv

TU Delft COVID-app: A tool to democratize CFD simulations for SARS-CoV-2 infection risk analysis

David Engler Faleiros [a], Wouter van den Bos [a,b,*], Lorenzo Botto [a], Fulvio Scarano [c]

[a] Faculty of Mechanical, Maritime and Materials Engineering (3mE), TU Delft, the Netherlands
[b] SDC Verifier, the Netherlands
[c] Faculty of Aerospace Engineering, TU Delft, the Netherlands

HIGHLIGHTS

- Improved accessibility of numerical simulations for SARS-CoV-2 infection risk analysis (the application)
- Input data for unsteady simulations of a person speaking with and without mask provided by PIV experiments
- Compilation of the relevant data for simulation of human expiratory activities (coughing, sneezing, breathing and speaking)
- Study case discusses the relative importance of different droplet sizes and the consequences of neglecting droplet evaporation

GRAPHICAL ABSTRACT

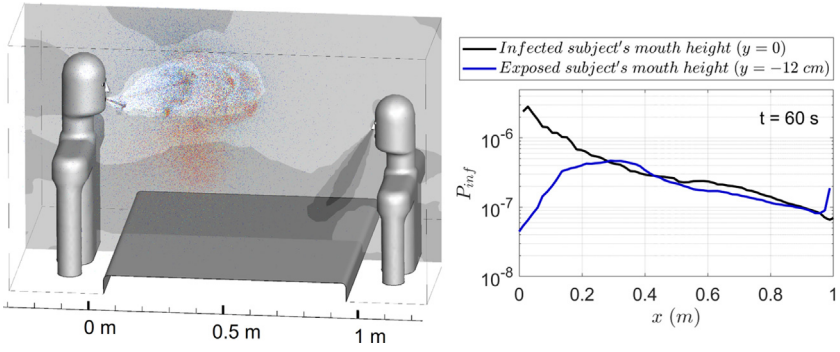

ARTICLE INFO

Article history:
Received 8 October 2021
Received in revised form 20 February 2022
Accepted 21 February 2022
Available online 25 February 2022

Editor: Warish Ahmed

Keywords:
COVID-app
Application
SARS-CoV-2 dispersion
COVID-19 simulation
Infection probability
Unsteady speaking

ABSTRACT

This work describes a modelling approach to SARS-CoV-2 dispersion based on experiments. The main goal is the development of an application integrated in Ansys Fluent to enable computational fluid dynamics (CFD) users to set up, in a relatively short time, complex simulations of virion-laden droplet dispersion for calculating the probability of SARS-CoV-2 infection in real life scenarios. The software application, referred to as *TU Delft COVID-app*, includes the modelling of human expiratory activities, unsteady and turbulent convection, droplet evaporation and thermal coupling. Data describing human expiratory activities have been obtained from selected studies involving measurements of the expelled droplets and the air flow during coughing, sneezing and breathing. Particle Image Velocimetry (PIV) measurements of the transient air flow expelled by a person while reciting a speech have been conducted with and without a surgical mask. The instantaneous velocity fields from PIV are used to determine the velocity flow rates used in the numerical simulations, while the average velocity fields are used for validation. Furthermore, the effect of surgical masks and N95 respirators on particle filtration and the probability of SARS-CoV-2 infection from a dose-response model have also been implemented in the application. Finally, the work includes a case-study of SARS-CoV-2 infection risk analysis during a conversation across a dining/meeting table that demonstrates the capability of the newly developed application.

1. Introduction

The severe acute respiratory syndrome coronavirus 2 (SARS-CoV-2), which causes the coronavirus disease 2019 COVID-19), is present in all sorts of bodily fluids (Wölfel et al., 2020). One of the main routes of human-to-human transmission of COVID-19 is through virion-laden

* Corresponding author at: Faculty of Mechanical, Maritime and Materials Engineering (3mE), TU Delft, the Netherlands.
E-mail address: w.vandenbos@tudelft.nl (W. van den Bos).

http://dx.doi.org/10.1016/j.scitotenv.2022.154143

droplets and aerosols of sputum or saliva of an infected person (Asadi et al., 2020; Zhang et al., 2020), expelled either orally or nasally through breathing, speaking, singing, coughing or sneezing (Bourouiba et al., 2014, Mittal et al., 2020, Gregson et al., 2021, Bahl et al., 2021). Virion-laden droplets can enter the body of a susceptible person through the mouth and nose (Mittal et al., 2020) (and possibly through the eyes, Kitazawa et al., 2021) via inhalation of aerosols, deposition of large droplets or contact with virus-contaminated objects (Goldman, 2020).

The physical process governing the transport of expelled droplets of sputum and saliva are mainly inertia, gravity, air resistance, and evaporation (Xie et al., 2007). Evaporation continuously reduces the droplets mass until they are reduced to their non-volatile fraction (*droplet nuclei*) (Liu et al., 2017). Large droplets are greatly influenced by gravity, following semi-ballistic trajectories (Bourouiba et al., 2014). Small droplets (aerosols) instead, are trapped within a hot and moist gas cloud generated by the expiratory activity, reaching significantly larger distances (7–8 m during a sneeze, Bourouiba, 2020) and remaining *airborne* for longer periods (minutes to hours). Wells (1934) defined large droplets as those reaching the ground prior to becoming droplet nuclei, while aerosols fully evaporate and become airborne. This threshold, reportedly within 60–100 μm (droplet diameter, Xie et al., 2007), depends on the person's height and mouth opening, the exhaled flow velocity, the ambient temperature and the relative humidity. Other works (Lelieveld et al., 2020; Klompas et al., 2020) and guidelines from the World Health Organization (WHO, 2014) use a more arbitrary definition for aerosols (droplets <5 μm), disregarding considerable part of the aerosol particle size distribution. This has been previously criticized in other works, where it was suggested the adoption of a threshold of 100 μm diameter to distinguish between droplets and aerosols (Prather et al., 2020).

The number of virions in a droplet depends on the droplet size and virus concentration. Assuming homogeneous concentration of virions in the saliva or sputum, then the number of virions is proportional to the droplet volume. For instance, the number of virions in 10 μm and 100 μm droplets is, respectively, 10^3 and 10^6 times that in a droplet of 1 μm diameter. Thus, deposition of large droplets, when successful, leads to high probability of infection. Aerosols, on the other hand, remain airborne for hours and spread over large spaces, enhancing the likelihood of airborne infections, especially in confined and poorly ventilated spaces (Bluyssen et al., 2021, Ren et al., 2021).

The potential of SARS-CoV-2 infection through airborne droplets was largely neglected in the beginning of the pandemic, gradually being recognized as a serious threat by governments, health organizations and scientists. The viability of SARS-CoV-2 in air has been firmly established (Van Doremalen et al., 2020; Meyerowitz et al., 2021). Isolated viable SARS-CoV-2 samples have been collected up to 5 m from patients (Meyerowitz et al., 2021) and the half-life was estimated to be 1.1–1.2 h, based on experiments with aerosols containing SARS-CoV-2 (Van Doremalen et al., 2020). Nevertheless, Klompas et al. (2020) argues that recovering “viral RNA from air does not prove aerosol-based transmission” and that “infection depends as well on the route of exposure, the size of inoculum, the duration of exposure, and host defences”. Epidemiological studies, however, do suggest the occurrence of SARS-CoV-2 infections through aerosols (Brlek et al., 2020; Shen et al., 2020; Li et al., 2021). The risk of airborne infection is reduced by avoiding close contact (1.5 m), as the concentration of aerosols reduces with distance from the infected person due to spreading and mixing of the exhaled flow with the ambient air (e.g. Bourouiba et al., 2014). However, distancing rules are insufficient to contain aerosol infection and the spread of aerosols carrying SARS-CoV-2 must be considered for effective engineering solutions and policy implementations.

Fluid dynamic experiments and simulations provide information on the routes of SARS-CoV-2 transmission and on the efficacy of prevention methods. Ventilation systems, for instance, have been tested experimentally using submillimetre soap bubbles injected through a mannequin's mouth (Bluyssen et al., 2021) and through computational fluid dynamics (CFD, Ren et al., 2021). Mask effectiveness has been investigated through flow visualizations (Tang et al., 2009; Arumuru et al., 2020; Staymates, 2020; Verma et al., 2020), through particle image velocimetry (PIV, Kähler and Hain, 2020) and through CFD (Khosronejad et al., 2020). Case studies of pathogen infection risk, based on CFD simulations, have also been performed in aircrafts (Gupta et al., 2011), hospitals (Bhattacharyya et al., 2020), during dialogues (Cortellessa et al., 2021), among others. Experiments through the addition of artificial aerosol tracers only yield information of the air motion (saliva droplets cannot be visualized in large-scales), lacking the level of detail needed for analysis of infection risk.

The uniqueness of each environment, however, hinders the generalization of case studies and prevention strategies. People act as sources of rising thermal plumes that significantly influence the ambient flow (Sun et al., 2021). Furthermore, the position of windows, doors, heaters and air-conditioners, the ambient temperature, the relative humidity, the existence of protection screens (shops), the use or absence of masks and people's clothing, all contribute to the routes of expelled droplets. Smart ventilation systems (Bhagat et al., 2020), for instance, aimed at air stratification in two layers (one hot and one cold), where droplets accumulate and are safely extracted near the ceiling, are more adequately implemented in a case-to-case basis. However, numerical simulations of human expiratory activities involve knowledge of data and models that can only be obtained through experiments and are not easily implemented, restricting the applicability of CFD simulations to scientific research and large corporations (e.g. aircraft manufacturers). Even for a person with the required technical background, collecting information on relevant models and data from the engineering and medical research is a daring and time-consuming task, which is incompatible with the necessary fast response demanded for a pandemic, and unfeasible for most small and medium size companies.

To overcome these difficulties, an application has been developed to enable computational fluid dynamics (CFD) users with limited knowledge of the physics of COVID-19 transmission to set up in a relatively short time complex simulations of virion-laden droplet dispersion. The tool, referred to as *TU Delft COVID-app*, considerably facilitates the implementation of unsteady simulations of the human expiratory activities in Ansys Fluent, a widely-used computational fluid dynamics (CFD) software. This allows architectural and engineering firms to calculate the probability of SARS-CoV-2 infection and optimize indoor spaces and their ventilation, for minimizing the rate of transmission. The application can also be used by the scientific community, for instance, when aiding governments at policy implementations. The necessary data for establishing the proper boundary conditions (e.g. air flow rate and direction, droplet concentration, size distribution of droplets, volatile fraction, temperature and relative humidity, viral load, among others) for coughing, sneezing, speaking and breathing are reviewed and the implementation procedures are described. In addition, Particle image velocimetry (PIV) measurements are performed of unsteady speaking without protection and wearing surgical masks to address the gaps in the reviewed data. Furthermore, a dose-response model (Watanabe et al., 2010) for estimation of the probability of infection and the filtration effect of surgical masks and N95 respirators are made available in the application. A case-study concludes this paper, where a dialogue across a dining/meeting table is simulated through the application, yielding the probability of infection among the attendees.

2. TU Delft COVID-app

The purpose of the TU Delft COVID-app is to facilitate the setup of simulations dealing with human-to-human SARS-CoV-2 infection in the widely-used CFD software Ansys Fluent. The application supports the CFD user step-by-step from the geometry design to the generation of user-defined functions (UDFs) that correctly emulate human expiratory activities.

In the process of geometry definition (Fig. 1), room size, temperature and relative humidity are specified, along with the size and coordinates of doors and windows. Additional parameters account for the number of people, their location, posture (sitting or standing) and orientation, gender, height, weight and clothing. Each person may be coughing, sneezing,

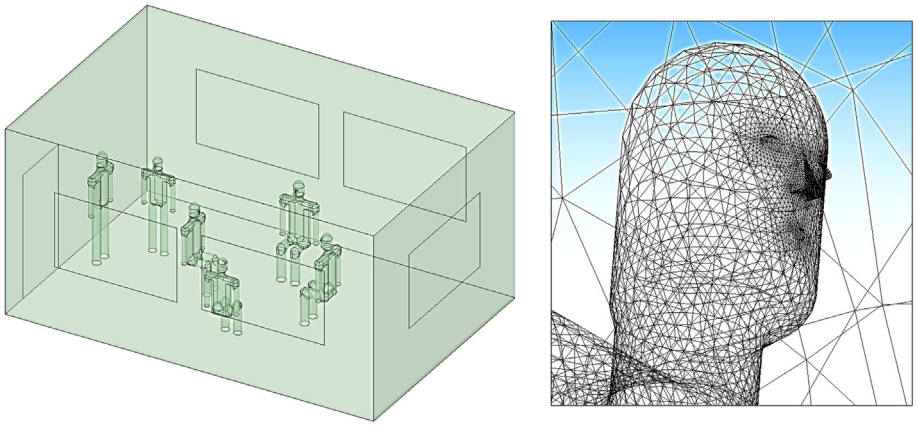

Fig. 1. Simulation geometry (left) created in Ansys Fluent using the TU Delft COVID-app. Right: mesh details near the face.

speaking or breathing through the nose. Surgical masks and N95 respirators can be chosen during speaking.

Following the user selection, the app detects the important boundaries (mouth, nostrils, eyes, body surface, windows, doors and walls) and defines the mouth opening, temperature of body parts and temperature and relative humidity of the exhaled air (Section 3.1). The transient air volume flow rate and flow direction at the mouth, during coughing and sneezing, or through the nose, while breathing, are defined (based on literature data) through the use of UDFs (Sections 3.2 and 3.3). The flow velocity components during unsteady speaking either unprotected or wearing a surgical mask are defined based on data obtained from the current PIV experiments (Section 6). The droplet size distribution for each expiratory activity is defined based on regression of experimental data reported in the literature (Section 3.4). The mass flow rate is defined based on the air flow rate and the mass concentration of saliva/sputum droplets (Section 3.4). The penetration of surgical masks or N95 respirators are defined by the app considering both penetration through the mask and through leakages (Section 4). Furthermore, the app calculates the probability of the exposed subject to become infected by the coronavirus based on a dose-response model (Section 5). An overview of the application capabilities is given on Table 1.

It is worth noting that the application is built in a flexible platform, where the equations used to define air flows, droplet distribution, mask penetration and the probability of infection can be easily updated as more accurate data become available from ongoing and future studies. The app can be downloaded on the SDC Verifier's website (TU Delft, 2021), partner of TU Delft in this project, where detailed information on the user interface is available, along with examples of simulations.

Table 1
Overview of the TU Delft COVID-app user-input parameters, simulation and output parameters.

User selection	Computed by the app
• Room size	• Room and bodies
• Windows and doors	o Scaled bodies
• Ambient conditions	o Mouth and nostril opening sizes
o Temperature	o Surface temperature
o Pressure	• Expired air
o Relative humidity	o Temperature
• Number of people	o Relative humidity
• People location, viewing angle and posture	o Flow direction
• Gender, height and weight	o Unsteady volume flow rate
• Clothing type	• Particle injections
• Expiratory activity	o Droplet size distribution
o Breathing	o Unsteady mass flow rate
o Speaking	o Particle initial velocity
o Coughing	• Surgical mask or N95 respirator
o Sneezing	o Air resistance due to mask
• Particle size	o Mask penetration (with leakage)
• Surgical mask or N95 respirator	• SARS-CoV-2 infection risk

3. Modelling of human expiratory activities

3.1. Human CAD model, temperature and relative humidity

Human CAD models have been designed for the COVID-app in both standing and sitting positions and are scaled according to the selected height. The mouth and nostril surface areas in square millimetres are given on Table 2.

The body temperature varies depending on the body part and the clothing. A recent study (Metzmacher et al., 2018) on skin surface temperature is used here as reference. The average values are summarized on Table 3.

The mean temperature and relative humidity of the exhaled breath, measured by Mansour et al. (2020), is about 33 °C and 72%, respectively.

3.2. Expired air flow rate during expiratory activities

The air flow rates during coughing (Gupta et al., 2009), sneezing (Busco et al., 2020) and breathing (Gupta et al., 2010) used in the COVID-app are reported concisely below in the notation of this paper. Only average flow rate for speaking (Gupta et al., 2010) or as a quasi-steady jet approximation from the constant repetition of strong syllables (Abkarian et al., 2020) has been reported in detail for use in simulations and is not reviewed here. The boundary conditions for unsteady speaking used in the COVID-app are based on experimental data reported on Section 6.

3.2.1. Coughing flow rate

The expelled air flow rate from 25 people (12 females and 13 males), while coughing, has been measured with a spirometer by Gupta et al.

Table 2
Surface area of mouth and nostril during coughing (Gupta et al., 2009), speaking and breathing (Gupta et al., 2010) and sneezing (Busco et al., 2020).

	Surface area			
	Mouth (mm^2)		Per nostril (mm^2)	
Activity	Male	Female	Male	Female
Coughing	400 ± 90	340 ± 140	–	–
Sneezing	130	–	–	–
Speaking	180	180	–	–
Breathing	120 ± 50	120 ± 70	70 ± 20	60 ± 10

Table 3
Body surface temperatures (rounded values from Metzmacher et al., 2018).

Ambient	Face	Bare chest	T-shirt	Sweater	Winter jacket
25°C	33–35°C	33°C	30°C	28°C	23°C

(2009). The authors characterized the volume flow rate of air $Q(t)$ with a 2-gamma distribution, as follows:

$$Q^*(\tau) = \frac{a_1 \tau^{b_1-1} e^{-\frac{\tau}{c_1}}}{\Gamma(b_1) c_1^{b_1}} + \frac{a_2 (\tau - 1.2)^{b_2-1} e^{-\frac{(\tau-1.2)}{c_2}}}{\Gamma(b_2) c_2^{b_2}} \quad (1)$$

where $Q^* = Q/Q_{peak}$ and $\tau = t/t_{peak}$. Q_{peak}, the *cough peak flow rate,* is reached at $t = t_{peak}$ (Fig. 2). The first term on the right-hand-side of Eq. (1) depends on the constants a_1, b_1 and c_1 (Table 4). The second term depends on the functions $a_2(V^*)$, $b_2(V^*)$ and $c_2(V^*)$, where $V^* = V_{cough}/(t_{peak}Q_{peak})$ is the dimensionless *cough expired volume*. The total air volume expired during one cough is given as:

$$V_{cough} = \int_0^{t_{cough}} Q(t)dt \quad (2)$$

where t_{cough}~0.6 s is the cough duration.

The authors then presented correlations for Q_{peak}, t_{peak} and V_{cough} (Table 5), depending on the gender, height h and weight m, closing the relations.

The velocity magnitude (Fig. 2, right) can be obtained by dividing the air volume flow rate (Fig. 2, left) by the mouth surface area given on Table 2.

3.2.2. Sneezing flow rate

Following the work of Gupta et al. (2009), Busco et al. (2020) measured the dynamic pressure $q(t)$ [Pa] during a sneeze and also fitted the data using a 2-gamma distribution:

$$q(t) = \frac{a_1 t^{b_1-1} e^{-\frac{t}{c_1}}}{\Gamma(b_1) c_1^{b_1}} + \frac{a_2 t^{b_2-1} e^{-\frac{t}{c_2}}}{\Gamma(b_2) c_2^{b_2}} \quad (3)$$

The authors only measured the sneeze of a single person and did not provide therefore any correlations with gender, height and weight. The constants are given on Table 6. The velocity magnitude is calculated as:

$$U(t) = \sqrt{\frac{2q(t)}{\rho}} \quad (4)$$

where ρ is the air density. The air velocity during sneeze (Fig. 3, right) for $\rho = 1.136$ ($T = 33.25$ °C, $p = 1$ atm, relative humidity RH = 71.6%) is one order of magnitude larger than that during coughing, reaching a peak velocity of 120 m/s at the mouth, which is about one third of the sound speed in air at normal temperature and pressure.

3.2.3. Breathing flow rate

Gupta et al. (2010) studied human breathing flow rate at rest using the same experimental techniques proposed in Gupta et al. (2009) (spirometer measurements, 12 females and 13 males). The authors reported a sinusoidal flow rate, where the amplitude and period during inhalation differs from that during exhalation. For a cycle in which inhalation precedes exhalation, the sum of volume flow rates through both nostrils during inhalation Q_{in} [l/s] (negative sign) and exhalation Q_{out} [l/s] are given as:

$$\begin{aligned} Q_{in}(t) &= -\frac{1}{2}\overline{Q}_{out}\omega_{in}T\sin(\omega_{in}t), && \text{for } 0 \le t < t_{in} \\ Q_{out}(t) &= \frac{1}{2}\overline{Q}_{out}\omega_{out}T\sin[\omega_{out}(t-t_{in})], && \text{for } t_{in} \le t < T \\ T &= t_{in} + t_{out}, t_j = \frac{30}{f_j}, && \omega_j = 2\pi\left(\frac{f_j}{60}\right) \end{aligned} \quad (5)$$

where j stands for either *in* or *out*, $\overline{Q}_{out}$ [l/s] is the mean expired flow rate, f_j [min^{-1}] and ω_j [s^{-1}] are the linear and angular frequencies, t_j [s] is the half period of either inhalation or exhalation and T [s] is the respiration period.

The parameters $\overline{Q}_{out}$ and f_j (Table 7) depend on the person's height [m], mass [kg] and body surface area A_{body} [m^2], which is given as (Bailey and Briars, 1996):

$$A_{body} = 0.16\, h^{0.42} m^{0.52} \quad (6)$$

The velocity magnitude (Fig. 4, right) can be obtained by dividing the air volume flow rate (Fig. 4, left) by twice the nostril surface area given on Table 2.

3.3. Flow direction

The direction of the exhaled air can be defined based on the two angles θ and ϕ between the symmetry axis of the expelled jet or puff and the horizontal lines on the side and front planes (Fig. 5), respectively. These angles have been estimated (Table 8) from the inspection of photographs of cigarette smoke exhaled by humans during coughing (Gupta et al., 2009) and breathing (Gupta et al., 2010).

The angle during a sneeze (Busco et al., 2020), measured based on the light scattering from laser-illuminated droplets, also accounted for the head movement and is given as a function of time:

$$\theta = \begin{cases} 40.7\sin(4.71\,t + 1.77) + 15.5\sin(13.5\,t + 2.19), & 0 \le t \le 0.24 \\ 13.7\log(t) + 17.9, & 0.24 < t \le 0.54 \end{cases} \quad (7)$$

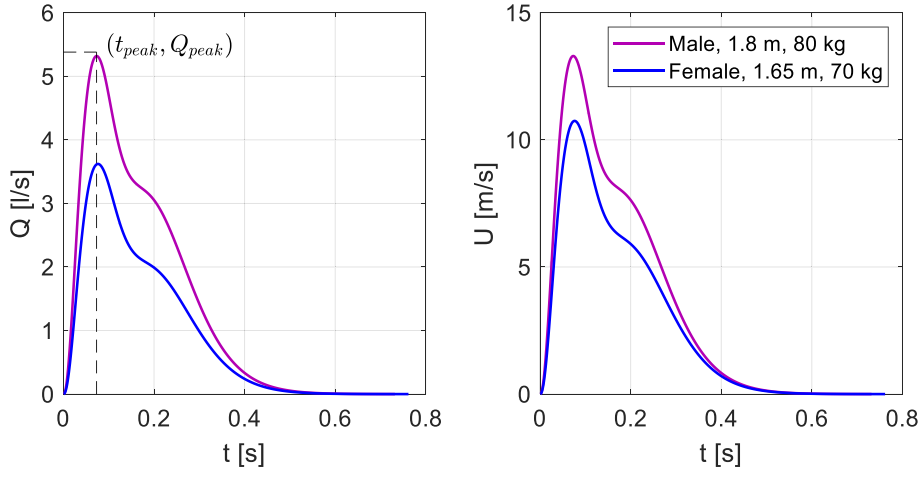

Fig. 2. Air volume flow rate (left) and velocity magnitude (right) during coughing, based on Gupta et al. (2009).

Table 4
Constants for calculating coughing volume flow rate from Gupta et al. (2009).

a_1	b_1	c_1	a_2	b_2	c_2
1.680	3.338	0.428	$\begin{cases} 0 & for\ \tau<1.2 \\ V^*-a_1 & for\ \tau\geq 1.2 \end{cases}$	$10.457 - 2.158\ V^*$	$\frac{1.8}{b_2-1}$

Table 5
Correlations for Q_{peak}, t_{peak} and V_{cough} from Gupta et al. (2009).

Gender	Q_{peak}[l/s]	t_{peak}[ms]	V_{cough}[l]
Male	$-8.9 + 6.4\ h$ [m] $+0.035\ m$ [kg]	$1.4\ Q_{peak}$ [l/s] + 65.9	$0.14\ Q_{peak}$ [l/s] + 0.3
Female	$-4.0 + 4.6\ h$ [m]	$3.2\ Q_{peak}$ [l/s] + 64.631	$0.2\ Q_{peak}$ [l/s] - 0.04

Table 6
Constants for calculating sneezing volume flow rate from Busco et al. (2020).

a_1	b_1	c_1	a_2	b_2	c_2
860.1	4	0.0235	674.4	9	0.028

The flow angle during speaking depends upon the pronounced syllable as described by Abkarian et al. (2020). To the authors' knowledge there is not yet sufficient data available to cover each syllable individually. Instead, in this paper the horizontal and vertical components of velocity while reading a passage are given as a function of time (Section 6.4).

3.4. Injection of sputum and saliva

Sputum and saliva are simulated as water liquid with 98.2% volatile content (Liu et al., 2017). This means that the droplet nuclei (droplets after complete evaporation) reduce to 1.8% of their initial volume (the diameter reduces to about one quarter of its initial value). The droplets initial velocities are set equal to that of the flow by the application through an UDF. The most important experimental data used as inputs for the simulations concerns the droplet size distribution and the mass flow rate.

3.4.1. Mass flow rate

The mass flow rate is usually measured indirectly through measurements of the total mass expelled during one event or of the droplet mass concentration C [kg/m^3]:

$$C = \frac{1}{V_{cell}} \sum_{i=1}^{n} \rho_d \frac{\pi}{6} d_{d,i}^3 \tag{8}$$

Table 7
Correlations for $\overline{Q}_{out}$, f_{in} and f_{out} from Gupta et al. (2010).

Gender	$\overline{Q}_{out}$ [l/s]	f_{in} [min^{-1}]	f_{out} [min^{-1}]
Male	$0.087\ A_{body}$[m^2]	$55.5–32.9\ h$ [m] $+0.26\ m$ [kg]	$77–45.4\ h$ [m] $+0.237\ m$ [kg]
Female	$0.077\ A_{body}$[m^2]	$46.4–18.9\ h$ [m]	$54.5–25.5\ h$ [m]

where V_{cell} [m^3] is the volume of a cell comprising n droplets, ρ_d [kg/m^3] is the droplet density and d_d [m] is the droplet diameter. Assuming the concentration to be constant, the mass flow rate can be estimated as:

$$\dot{m}\ (t) = \overline{C} Q(t) \tag{9}$$

where $\overline{C}$ is the ensemble averaged concentration obtained from experiments. Direct measurements of mass concentrations are used to obtain the mass flow rate during breathing (Gregson et al., 2021).

Techniques that physically capture the total expelled mass are also suited for obtaining the average mass concentration when the total air volume is known. This method is used here for obtaining the mass concentration during coughing, sneezing and speaking.

The total mass during coughing has been measured by weighing a respiratory mask (6.7 mg, Zhu et al., 2006; 1.1 mg, Xie et al., 2009) or plastic bag (4.2 mg, Xie et al., 2009) before and after several coughs and averaging the weight difference. Measurements by Duguid (1946) agrees closely to that of Zhu et al. (2006), yielding 7.5 mg during coughing and about 550 mg during sneezing. Xie et al., 2009 also reports measurements of the total mass of saliva expelled while counting from 1 to 100: 18.7 mg and 79.4 mg, when weighing a mask and a plastic bag, respectively. The presence of either leakage (mostly mask) or water vapour condensation (plastic bag) affects the results.

The exhaled air volume during a single cough or sneeze is obtained by integrating the volume flow rate during the event duration. For speaking, the average volume rate during counting from 1 to 10 is used (Gupta et al., 2010):

$$\begin{aligned} \bar{Q}_{male}\ [\mathrm{l/s}] &= 0.38\ A_{body}\ [\mathrm{m^2}], \\ \bar{Q}_{female}\ [\mathrm{l/s}] &= 0.30\ A_{body}\ [\mathrm{m^2}], \end{aligned} \tag{10}$$

which is integrated in time to yield the total expired volume V_{1-100} while counting from 1 to 100.

To obtain the mass concentration, the expired volume is estimated based on the participants of the saliva mass measurements of Xie et al., 2009. Considering three Chinese males (1.75 m, 73.5 kg, $\overline{A}_{body}$ = 1.9 m^2) and four females (1.63 m, 62.2 kg, $\overline{A}_{body}$ = 1.69 m^2)

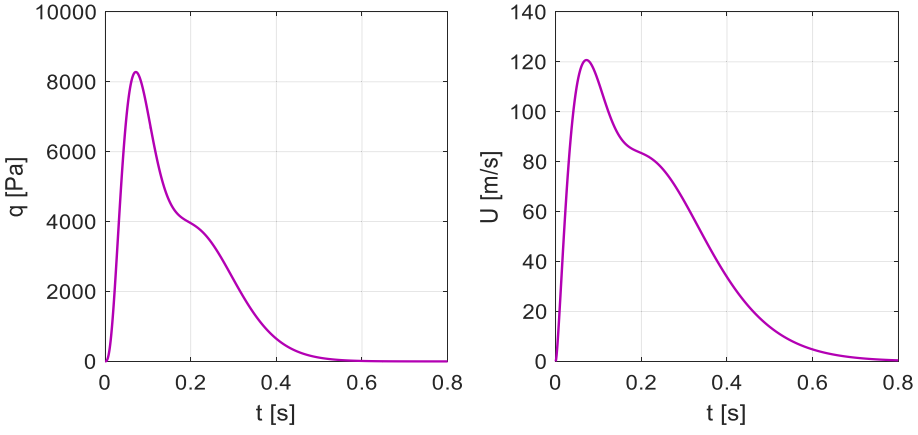

Fig. 3. Dynamic pressure (left) and velocity magnitude (right) during sneezing, based on Busco et al. (2020).

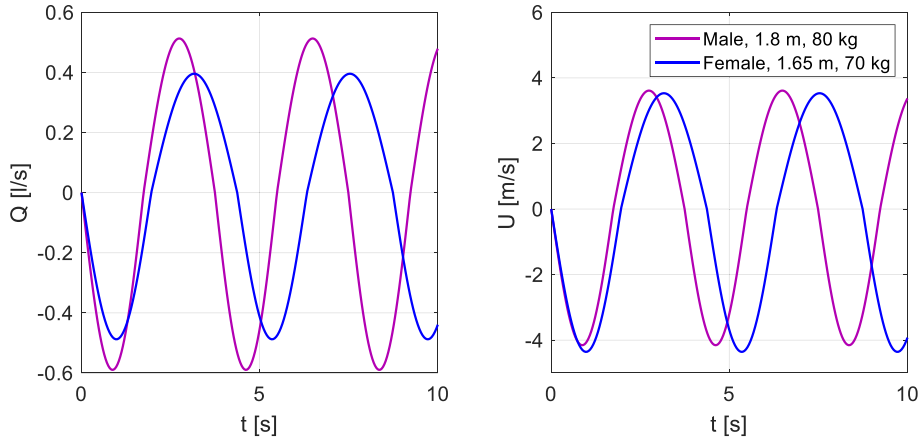

Fig. 4. Breathing volume flow rate (left) and velocity magnitude (right) based on Gupta et al. (2010).

(Rodriguez-Martinez et al., 2020), the weighted average of the expired volume is $\overline{V}_{1-100} = 59.9$ l.

Based on the above, the average mass concentration for coughing, sneezing, speaking and breathing, used to calculate the mass flow rate from Eq. (9), are given on Table 9.

3.4.2. Droplet size distribution

The Rosin-Rammler particle size distribution (Vesilind, 1980), also known as Weibull distribution, was first applied by Rosin and Rammler in 1933 while studying the fineness of powdered coal. Currently, it is used in spray technology, meteorology, aerosol science, among others (Alderliesten, 2013). Its cumulative distribution function used for fitting measurements of the cumulative mass fraction of particles smaller than d, is given as:

$$Y(d) = 1 - \exp\left(-\frac{d}{d_0}\right)^n \tag{11}$$

where n is the *uniformity constant* and d_0 is the *characteristic particle size*. The definition of d_0 follows from Eq. (11): it represents the diameter threshold that separates the particles in two size groups, where the smaller particles ($d \leq d_0$) amount to 63.2% ($1 - 1/e$) of the total mass.

Measurement data of the particle size distribution during speaking (Chao et al., 2009; Duguid, 1946), fitted with Eq. (11), is shown in Fig. 6. Notice that two curve fits are used: one for $d_d \leq 50$ μm, prioritizing the data from Chao et al., 2009, and another for $d_d > 50$ μm using both data combined. Dividing the data in two size ranges significantly improves the curve fits, even when a single dataset is used (see Fig. 7 for sneezing).

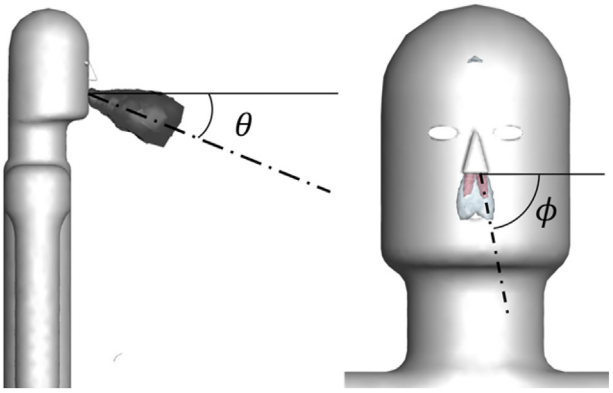

Fig. 5. Definition of exhaling direction on side (left) and front (right) views.

The fitting parameters and datasets used for all expiratory activities are listed on Table 10.

The Rosin-Rammler distribution is the standard option available in Ansys Fluent, requiring the user to provide only d_0 and n, however, the particle diameters are automatically selected within the selected range: $[\min d_d, \max d_d]$. In the COVID-app the user has more control and may select as many diameter ranges $[d_{d,\,i}, d_{d,\,i+1}]$ as deemed necessary, where each range is represented by its mean diameter and its mass fraction is given as,

$$\gamma_{d,i} = \frac{m_{d,i}}{m_{tot}} = [Y(d_{d,i+1}) - Y(d_{d,i})] \tag{12}$$

$m_{d,\,i}$ is the mass of all droplets within the range $[d_{d,\,i}, d_{d,\,i+1}]$ and m_{tot} is the mass of all expelled droplets. Thus, only the part of the particle distribution of interest is simulated (e.g. up to 100 μm diameter for airborne transmission) and represented by the mean diameters of the chosen diameter intervals. The diameter selection process is described in Fig. 8.

In addition, the use of two Rosin-Rammler distributions to fit the data (Table 10) improves the accuracy of the estimated mass fraction of each range with respect to the standard option in Fluent. The mass flow rate per particle diameter range becomes:

$$\dot{m}_{d,i}(t) = \gamma_{d,i}\overline{C}Q(t) \tag{13}$$

4. Surgical mask and N95 respirator penetration

Mask penetration is a measure of mask efficiency, based on the droplet concentration upstream and downstream of the mask. Many studies only considered droplet penetration through the mask (Qian et al., 1998; Lee et al., 2005; Ardon-Dryer et al., 2021), neglecting droplets escaping through leakages between the mask and the subject's face. The penetration of surgical mask and N95 respirator has been measured by Grinshpun et al. (2009) and Cho et al. (2010) using mannequins that simulated real human breathing patterns, with and

Table 8
Flow direction during coughing (Gupta et al., 2009), breathing (Gupta et al., 2010) and Sneezing (Busco et al., 2020).

	θ	ϕ
Coughing	27.5°	90°
Exhaled breath (mouth)	4°	90°
Exhaled breath (nose)	60°	69°
Sneezing	Eq. (7)	90°

Table 9
Average mass concentration $\overline{C}$ (mg/l) for coughing, sneezing, speaking, breathing in and out through the nose (n/n), and breathing in through nose and out through mouth (n/m). a Zhu et al., 2006: average of three male subjects ($\overline{h}$ = 1.72 m, $\overline{m}$ = 68 kg). b Gupta et al., 2009: Eq. (2) (male, h = 1.72 m, m = 68 kg). c Duguid (1946): one sneeze. d Busco et al. (2020): Eqs. (3) and (4). e Xie et al. (2009), average of both weighing methods (18.7 mg for mask and 79.4 mg for plastic bag). f Gupta et al. (2010), Eq. (10). g Gregson et al. (2021).

	Coughing	Sneezing	Speaking	Breathing (nose/nose)	Breathing (nose/mouth)
Total Mass (mg)	6.70 [a]	550 [c]	49.05 [e]	–	–
Total Volume (l)	0.91 [b]	4.41 [d]	59.9 [f]	–	–
Avg. conc. $\overline{C}$ (mg/l)	7.34	124.72	0.82	9.7×10^{-8} [g]	1.6×10^{-7} [g]

without leakage (the latter was achieved by gluing the mask to the face of mannequin). These studies have shown that the penetration of droplets due to leakage is the most significant. The total penetration through the mask and leakage is shown in Fig. 9. The following empirical fits for surgical masks and N95 respirators, respectively, are suggested:

$$P_{mask}(\%) = 50.3 \exp -\left(\frac{d_d\,[\mu\text{m}] + 0.886}{2.2}\right)^2$$
$$P_{N95}(\%) = 5.71 \exp -(0.787 d_d\,[\mu m]). \quad (14)$$

Eq. (14) is used in the COVID-app for correcting the mass flow rate of droplets. Unfortunately, Grinshpun et al. (2009) only measured penetration of sub-micrometre droplets, while Cho et al. (2010) limited their measurements to the penetration of N95 respirators for particles of up 4 μm diameter. Therefore, the maximum droplet diameter that may be found downstream of the mask/N95 is found through extrapolation of the dataset from Cho et al. (2010) for the N95 respirator and assumed to be the same for the surgical mask.

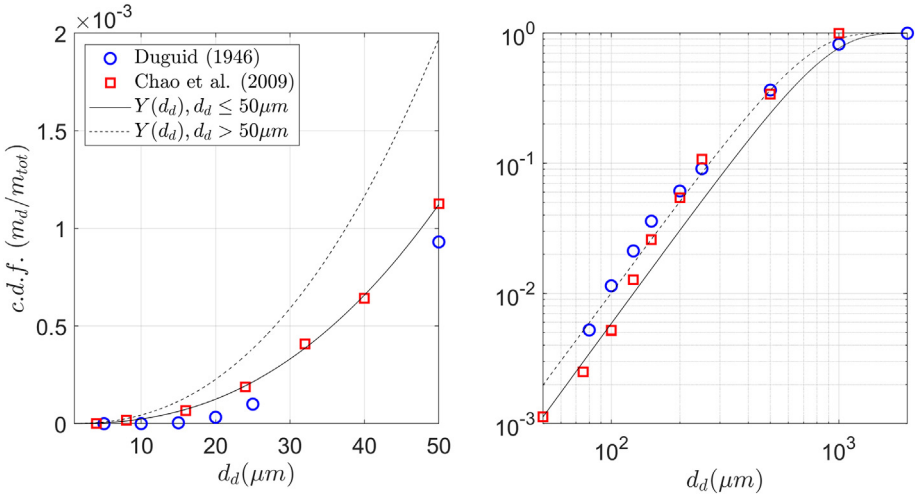

Fig. 6. Cumulative distribution function for the mass fraction of droplets generated during speaking.

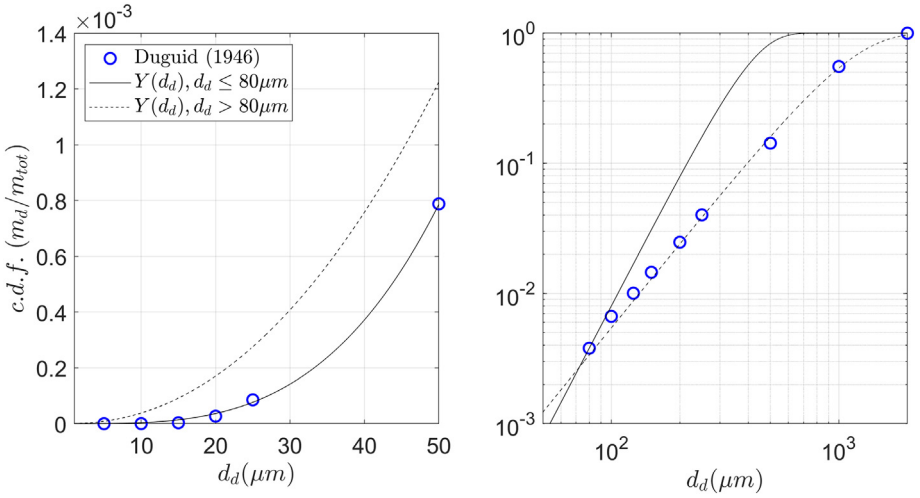

Fig. 7. Cumulative distribution function for the mass fraction of droplets generated during sneezing.

Table 10
Experimental data sets and fitting parameters used to fit the cumulative mass distributions of droplets generated during speaking, breathing through mouth, coughing and sneezing.

	Experimental data	Data size Range [μm]	d_0 [μm]	n
Speaking	Chao et al. (2009)	[2, 50]	850	2.39
	Chao et al. (2009)	[2,2000]	700	2.36
	Duguid (1946)			
Breathing (mouth)	Gregson et al. (2021)	[0.5, 1.9]	1.63	2.87
		[1.9, 13]	1.25	0.78
Coughing	Chao et al. (2009)	[2, 50]	1640	2.13
	Chao et al. (2009)	[50, 2000]	860	2.40
	Duguid (1946)			
Sneezing	Duguid (1946)	[5, 80]	420	3.35
		[80, 2000]	1130	2.15

5. Probability of infection

The probability of infection is calculated based on the dose-response model (Watanabe et al., 2010):

$$P_{inf}(d) = 1 - e^{-d/k} \tag{15}$$

where d is the viral dose given in plaque forming units (PFU) and k is the dose leading to an infection probability of 63.2%. Watanabe et al. (2010) estimated $k = 410$, based on a study of intranasal inoculation of mice with SARS-CoV. The model should be updated as more accurate estimates of k are obtained for SARS-CoV-2.

The number of SARS-CoV-2 RNA copies N penetrating a body through inhalation of droplets of saliva or sputum is given as:

$$N = \overline{c}_v \sum_{i=1}^{n} \frac{\pi}{6} d_{d,i}^3 \tag{16}$$

where n is the number of droplets inhaled and c_v is the average number of RNA copies per unit volume. Average and maximum viral load in the sputum of hospitalized patients with COVID-19 has been assessed to be 7 billion and 2.35 trillion RNA copies per litre (Wölfel et al., 2020), respectively. The actual number of RNA copies changes depending on the number of days since the onset of symptoms (Wölfel et al., 2020). For simplicity, only the average value is implemented in the COVID-app. The viral dose d is then estimated from the ratio of RNA copies to infectious

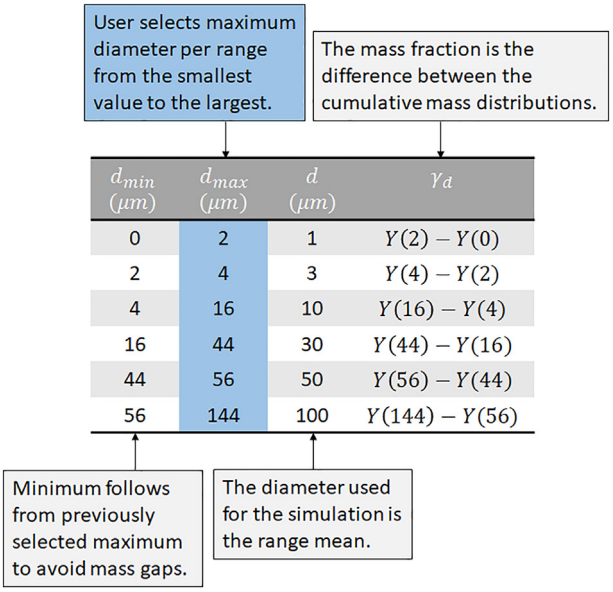

Fig. 8. Diameter selection process within the TU Delft COVID app.

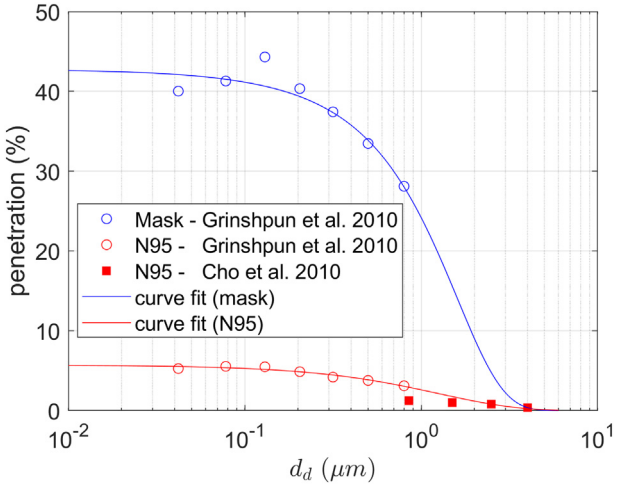

Fig. 9. Surgical mask and N95 penetration (including leakage). Data used for the curve fits: Grinshpun et al. (2009) and Cho et al. (2010), obtained from a person breathing at rest.

units (N/d) of approx. 16,000 (obtained from the compilation of several measurements of both quantities by Sender et al. (2021).

In Ansys Fluent, the number of RNA copies crossing through a surface (e.g. mouth, nostrils and eyes) may be monitored, yielding a direct measure of the probability of infection. In addition, $P_{inf}(d)$ may be estimated on the entire domain at all times, by assuming the presence of a breathing person at all points in space. In this case, Eq. (16) becomes:

$$N = \frac{c_v \overline{Q}_{in}}{\rho_d} \int_0^{t_{exp}} C\left(\vec{x}, t\right) dt \tag{17}$$

where $\overline{Q}_{in}$ is the average breathing volume flow rate during inhalation, $C\left(\vec{x}, t\right)$ is the droplet concentration as a function of time t and space $\vec{x}$, and t_{exp} is the time a subject has been exposed to the infected droplets. Based on Eq. (5) and on the European average height and weight (male: 1.79 m, 85.5 kg; female: 1.65 m, 70.5 kg; Rodriguez-Martinez et al., 2020), the average European inhalation volume flow rate while at rest is 0.14 l/s and 0.18 l/s for male and female, respectively.

Furthermore, it is worth noting that virus viability may play a role on the probability of infection estimation. The half-life of SARS-CoV-2 in air has been measured to be longer than 1 h (Van Doremalen et al., 2020; Morris et al., 2021). Morris et al. (2021) have shown that the SARS-CoV-2 viability depends on the ambient temperature and relative humidity, being approximately 1.5 h for RH = 6.5% and T = 27 °C, and longer than 24 h for RH = 40% and T = 10 °C. Therefore, for short simulations lasting for less than 1 min, the decay of SARS-CoV-2 within airborne aerosols is less than 1% and can be neglected.

6. PIV measurements during speaking

In this section, Particle image velocimetry (PIV) experiments are performed to obtain the unsteady flow velocity and direction during speaking, with and without a surgical mask. The main reason for performing these experiments is to be able to reproduce similar flow patterns of unsteady speaking in numerical simulations, where saliva droplets can be accurately modelled and observed. Therefore, the velocity measurements are used to estimate the air velocity at the mouth exit, required while defining the simulation boundary conditions.

6.1. Experimental setup

PIV measurements were performed at the TU Delft's laboratories to study the air flow exhaled during human expiratory activities. The setup

(Fig. 10) consists of an sCMOS camera from LaVision (2560 × 2160 pixels) coupled with a Nikon objective lens (35 mm focal length), an Nd:YAG Quantel laser (Evergreen, 200 mJ per pulse) and a smoke generator typically used for PIV measurements in wind tunnels. The laser sheet (2–3 mm thickness) was formed from below the mouth, passing through the subject's mid-plane. The sCMOS camera was positioned approximately at the subject's mouth height, at a distance of 80 cm from the laser sheet, with the objective's axis perpendicular to it. The image magnification was 0.05, rendering a field of view of 30 cm (height) x 36 cm (width). The image resolution was 0.14 mm/px. Images were acquired in frame-straddling mode (double frame, single exposure) at 10 Hz, with a time interval of 500 μs between frames.

The subject (male, 32 years old, 1.84 cm, 80 kg) was protected against the laser light by safety goggles and a black screen positioned in front of him (not shown), with a 5 cm diameter opening for the mouth exhaled air. A three-centimetre long circular cylinder of the same diameter was positioned at the opening to help positioning the head and to block the laser light from below. The head positioning was done with the subject's nose slightly touching the upper surface of the cylinder. Therefore, inhalation and exhalation through the nose did not influence the measured flow velocities. The entire setup, including the subject, was encompassed by a black tent (about 15 m^3), whose main objective was to contain the smoke. The entire tent was filled with smoke by turning the smoke generator for about 2 s, with the tent closed, and waiting for about 10 min for the smoke to become homogeneously spread.

Three different expiratory activities were measured: breathing in through nose and out through mouth, breathing in and out through mouth, and speaking. Each activity was recorded for the duration of 50 s (500 images), which comprised about 5 respiratory cycles. The speaking activity consisted of reciting an excerpt of the rainbow passage (Fairbanks, 1960), a speech often used for the study of voice and articulation and representative of the multiple sounds of the English language:

"When the sunlight strikes raindrops in the air, they act as a prism and form a rainbow. The rainbow is a division of white light into many beautiful colours. These take the shape of a long round arch, with its path high above, and its two ends apparently beyond the horizon. There is, according to legend, a boiling pot of gold at one end. People look, but no one ever finds it. When a man looks for something beyond his reach, his friends say he is looking for the pot of gold at the end of the rainbow."

6.2. Data processing and uncertainty

An example of raw image from the PIV measurements is shown in Fig. 11. The images were processed via cross-correlation analysis, using the software DaVis 8.4 from LaVision. The final interrogation window was 48 × 48 pixels (7 × 7 mm2) with 75% overlap, yielding about 160 × 200 vectors per image. Typical uncertainty of a PIV displacement measurement is 0.1 px (Raffel et al., 2018). The velocity magnitude close to the mouth varied in the range of 1–5 m/s (3–18 px). Thus, the uncertainty of the instantaneous velocity is estimated to be within 0.5–3%.

6.3. Time-averaged flow velocity

The mean horizontal u [m/s] and vertical v [m/s] flow velocity components measured without mask (top) and wearing a surgical mask (bottom) are shown in Fig. 12. The mean horizontal flow velocity near the mouth while unprotected is about 0.2 m/s and remains larger than 0.1 m/s up to 30 cm downstream of the mouth. The flow is somewhat bent upwards at an average angle with the horizontal direction of about 15° and vertical velocity of approximately 0.05 m/s. This is a consequence of the majority of the syllables resulting in a puff being expelled slightly upwards. However, the jet buoyancy also contributes to a positive vertical velocity. From Fig. 12 (top-left) it can also be observed that puffs moving upwards are attached to the upper wall of the tube passing through the protection screen opening (Fig. 11). Likewise, puffs moving downwards are attached to the bottom wall. This effect resulted in two distinguished sources of exhaled air, yielding in a larger lateral spreading of the flow.

The use of masks reduces the flow velocity by an order of magnitude. The mean horizontal velocity near the mouth is about 0.03 m/s, one order of magnitude smaller in comparison to that without mask. The vertical velocity is also reduced as a consequence of the mask and is below 0.01 m/s near the mouth. The loss of momentum in the horizontal direction enhances the influence of buoyancy. At the mouth, the flow is expelled at about 45° with the horizontal direction, rising at steeper angles as the horizontal momentum decrease, and remaining significantly closer to the body. The influence of speaking on the average flow velocity while wearing a mask is barely noticeable farther than 20 cm from the mouth.

6.4. Volume flow rate and velocity at the mouth

In this section the measurements of instantaneous velocity downstream of the mouth are used to estimate volume flow rate of air and, consequently, the flow velocity at the mouth. This task is not as straightforward as in the case of a jet, because the instantaneous flow field during speaking is composed of multiple puffs formed by different syllables that are expelled at different velocity magnitude and direction. When the velocity field in the horizontal direction at any time instant is sampled near the mouth (dashed rectangle, Fig. 13 left), the resultant 2D velocity profile (Fig. 13, right) may be seen as the superposition of several Gaussian curves, which is interpreted as the flow resultant from the combination of recently expelled puffs (forward flow), intercalated with air inhalation through the mouth (backward flow).

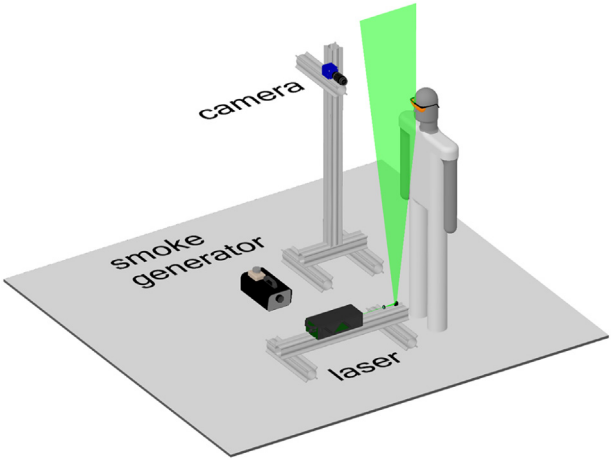

Fig. 10. PIV experimental set-up.

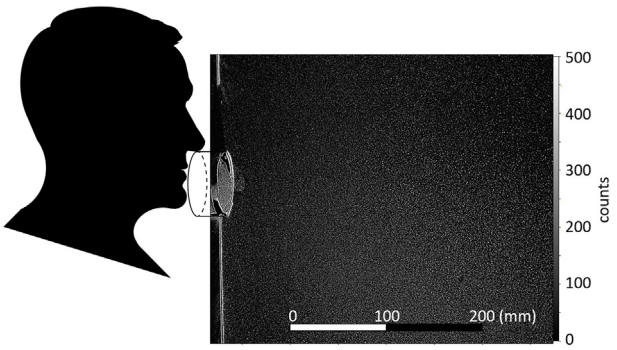

Fig. 11. Raw image from PIV measurements.

Assuming that each Gaussian curve may be revolved around its symmetrical axis to yield the two-dimensional velocity deficit in the x-plane, the volume flow rate at the mouth is obtained from mass conservation, which in incompressible flows is given as:

$$Q_{mouth} = \overline{u}_{mouth} A_{mouth} = \int_0^{2\pi} \int_0^{r_e} u(r)\, r\, dr\, d\theta \tag{18}$$

where $\overline{u}_{mouth}$ is the spatial avegescrage velocity for a mouth opening area A_{mouth}, $u(r)$ is the velocity deficit, r is vertical distance to the gaussian centre and θ is the angle from 0 to 2π along the perimeter of the circular rings of width dr. The Gaussian edge r_e limiting the integration is arbitrarily defined as the point where the velocity reaches 0.01 m/s. Eq. (18) only shows the contribution to the flow rate of a single Gaussian used during the curve fitting of the velocity profile. The total flow rate is obtained by summing the contribution of all Gaussians curves (all puffs and breaths).

Eq. (18) yields only the horizontal velocity component. The vertical velocity component is obtained from the average velocity ratio $\overline{v/u}$ obtained within the dashed-rectangular area near the mouth (Fig. 13 left). During this procedure small values of u ($u < 0.005$ m/s) are neglected to avoid unrealistic large v/u ratios.

The velocity components at the mouth during the 45 s of measurements with and without mask are shown in Fig. 14 (data points given in supplementary material). The velocity magnitude at the mouth without mask remains below 5 m/s for most measurements, reaching about 7–8 m/s in a dozen of cases. There is only a single occurrence of the horizontal velocity overcoming 10 m/s. Similarly to the results of average velocity fields, the velocity at the mouth without mask are about tenfold of that while wearing a mask. It is also noted that, when wearing mask, the velocity magnitude during backflow (breathing) is higher than during forward flow (puffs).

7. Case study: SARS-CoV-2 infection risk during a conversation

The TU Delft COVID-app is demonstrated through a case study of two people having a conversation without any protective mask across a small table (mouth-to-mouth distance of one metre), representing the situation of two friends in a restaurant or two colleagues during a meeting. Although, only a short simulation of 1 min is performed, in which the infected person speaks for a quarter of the time, the results are extrapolated in time, assuming a reoccurring pattern, to give the probability of infection after a few hours.

7.1. Simulation set-up

The transient simulations were set up in Ansys Fluent using the TU Delft COVID-app. The two subjects, one male 1.80 m and 80 kg and one female 1.65 m and 70 kg (standard app CAD models at sitting position are scaled according to their height) (Fig. 15). The male is infected with SARS-CoV-2 and releases saliva droplets (modelled as water droplets) containing SARS-CoV-2 virions (7×10^9 RNA copies per litre, Wölfel et a. 2020) while speaking. The male speaks for the first 15 s, followed by 45 s of normal breathing (simulation ends at 60 s). Particles are only released during speaking. The female breathes at regular pace while being exposed to the infected droplets expelled by the male. The breathing patterns are shown in Fig. 4. The flow velocity during speaking follows the experimental data (Fig. 14, left). Five different droplet diameters have been chosen for this simulation: 1, 3, 10, 30 and 50 μm, representing mainly aerosol transmission. Each particle diameter is injected with a mass-flow rate obtained from Eq. (13).

The simulated volume of $1 \times 1 \times 1.5$ m^3 (height × width × length) was gridded using tetrahedral elements of 10 cm far from the bodies and table, using ANSYS Fluent *advanced size functions* on proximity and curvature (normal angle of 15°). In addition, the mesh is further refined near the eyes, mouth and nose to 2.5 mm and on the nostril surface to 1.5 mm (Fig. 1, right). From a grid convergence analysis, where two grid refinements (factors of 2 and 4) are used to perform the Richardson extrapolation (Roache, 1998), the error in the estimation of second-order statistics of velocity due to discretization is calculated to be less than 1% (Appendix B).

The Navier-Stokes equations are solved with a pressure-based solver, using the *coupled* pressure-velocity coupling scheme and a second-order implicit formulation with a Courant Number ($C = u\Delta t/\Delta x$) of 25. An adaptative time stepping scheme is implemented through a user-defined-function, based on the Courant Number, the minimum mesh length ($\Delta x \sim 0.5$ mm) and the velocity at the mouth of the infected person, limited to a maximum time step of 25 ms. The turbulence is modelled using the RANS-based Shear Stress Transport (SST) $k-\omega$ model as it ensures a proper selection of the $k-\omega$ and $k-\varepsilon$ zones without user interaction (Menter et al., 2003) and has been chosen as default for the application.

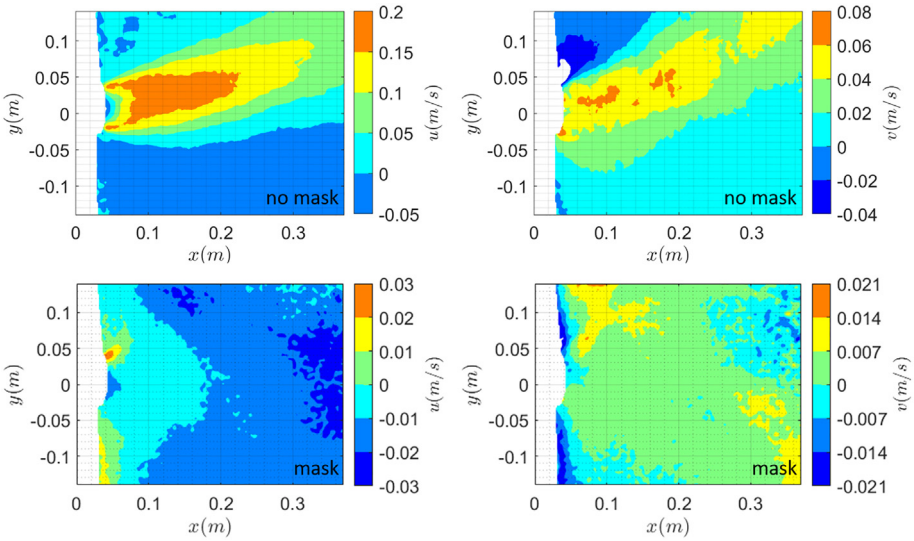

Fig. 12. Air flow produced by a speaking person: time-averaged horizontal (left) and vertical (right) velocity components without protection (top) and wearing a surgical mask (bottom). The flow is from left to right. The origin of the coordinate system is at the estimated position of the person's mouth based on the position of the laser protection screen (Fig. 11). The colour bar limits are adjusted for clear visualization.

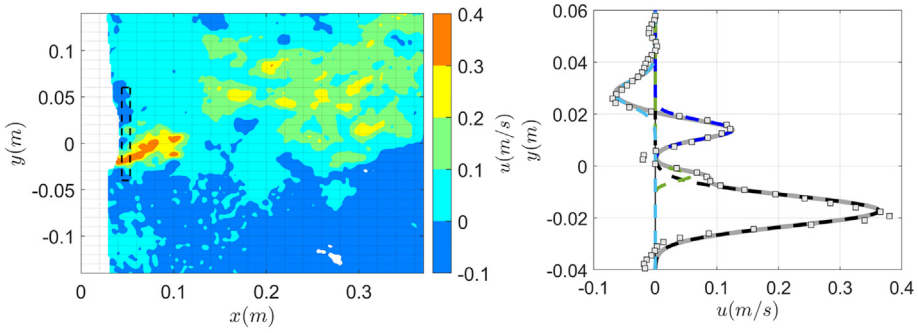

Fig. 13. Left: instantaneous velocity field measured with PIV while reciting the rainbow speech. Right: Vertical profile from the dashed rectangle.

The particle behaviour is simulated from a Lagrangian perspective. The equations of particle motion (Mei, 1996) only consider the inertial term, quasi-steady drag and gravity force. The drag coefficient is calculated from the empirical relations of Morsi and Alexander (1972). The DPM boundary conditions are given on Table 11.

For demonstration purposes, the energy equation is not included. This is equivalent to the situation of a hot day (about 33 °C, same temperature of the exhaled breath) in air saturated with water (relative humidity of 100%), where buoyancy effects are negligible, and evaporation does not occur. Droplet evaporation is, however, an important parameter and should

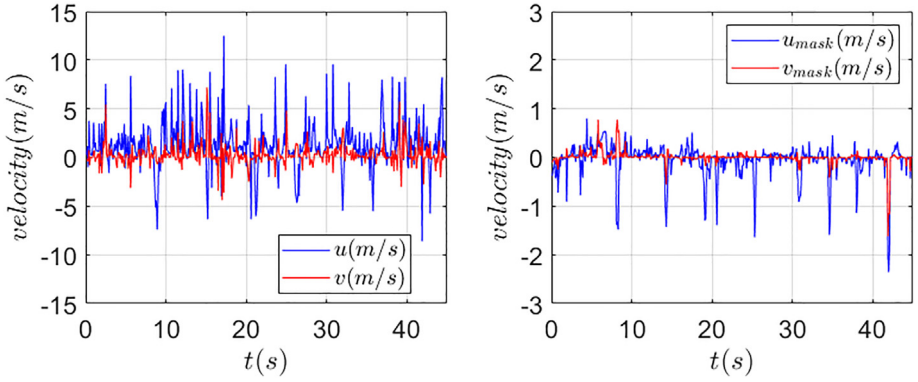

Fig. 14. Instantaneous velocity components at the mouth during speaking without mask (left) and wearing a surgical mask (right).

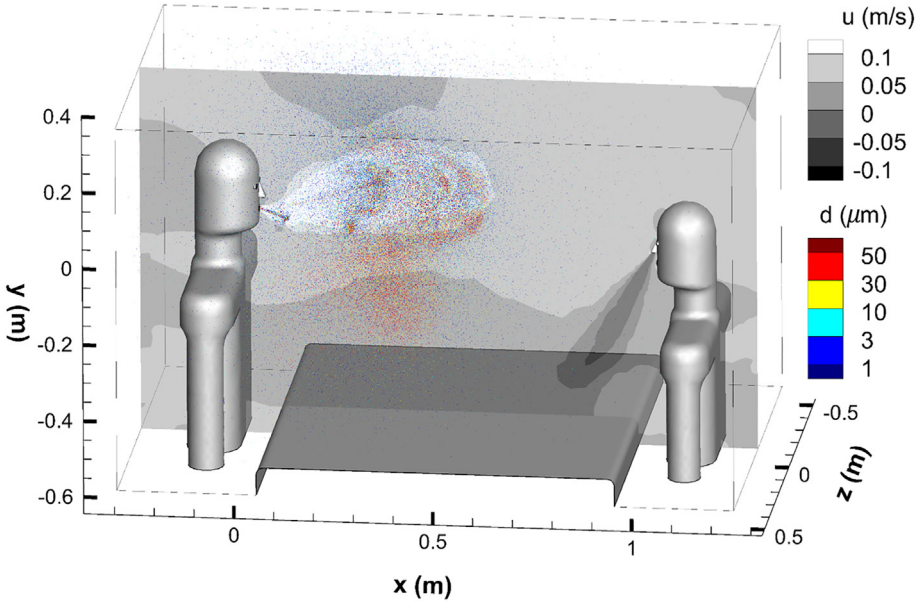

Fig. 15. Simulation of a conversation across a dining/meeting table. The male (left) is infected with SARS-CoV-2, speaks for 15 s followed by 45 s of breathing. The female (right) breaths during the entire simulation. The horizontal velocity contours are shown in the plane $z = 0$, while the droplets are plotted over the full simulated volume, delimited by the black dashed-lines.

be considered for more accurate calculations (this option is also available in the COVID-app, with the only drawback of longer processing times).

7.2. Average flow velocity: comparison with experiments

The average flow velocity during 15 s of speaking is shown in Fig. 16. The maximum average velocity near the mouth is about two-fold that obtained from the experimental data (Fig. 12, top). A more quantitative comparison is performed along a vertical profile at 20 cm downstream from the mouth (Fig. 17). The streamwise and transverse components of the average velocity during the simulations are slightly overestimated and underestimated, respectively (peak averages velocities are approximately 20% higher and 30% lower, respectively).

There are a few sources of uncertainty in the measurements that could explain the observed differences. One source is due to flow attachment in the top and bottom of the cylinder attached to the mouth during the experiments (Fig. 12, top-left), resulting in a wider spread of the average "jet" (in fact, it is the average flow of several puffs) and, consequently, a lower average velocity. Another source of uncertainty is the translation of velocity measurements a few centimetres from the mouth to a volume flow rate, and, subsequently, to a velocity inlet based on a mouth opening area. The main issues in this process was the lack of time resolution in the measurements and the necessity of having a protection between the person and the measurements for safety reasons. These two facts combined meant that the velocity measurements was a mixture of several pronounced syllables a few centimetres away from the mouth, which required assuming that the velocity profile was a mixture of distinguishable Gaussians (one for each syllable), yielding the 3D velocity profile through revolution around their axis of symmetry (Section 6.4). Measurements near the mouth (preferably in 3D) with higher temporal resolution would yield better input data for the simulations.

Additionally, the mouth opening during the experiments was not measured and was assumed to be 120 mm^2, based on measurements of mouth opening during breathing (Gupta et al., 2010) and sneezing (Busco et al., 2020). However, during speaking, Gupta et al., 2010, estimated an average value of 180 mm^2. Had the latter value been used during the simulations, the mouth velocity would be 2/3 of the simulated value.

Nevertheless, the differences in average velocity between experiments and simulations are most likely within natural biological differences in flow velocity during speaking found across different individuals. Thus, the differences found are deemed acceptable for this study, which did not aim at representing a universal speaking pattern. Higher velocities during the simulation should yield more conservative risks estimates with respect to physical-distancing rules.

7.3. Probability of infection

The probability of infection is estimated directly from Eq. (15) and by tracking all the inhaled particles through the nostrils (Fig. 18, left) —the cumulative number of inhaled RNA copies of SARS-CoV-2, the corresponding dose values and probability of infection every 5 s of the simulation are given in Table A1.1 (Appendix A). In addition, the probability of infection is estimated at all points in space based on the average inhalation flow rate (Fig. 19) from Eqs. (15) and (17). The two methods offer different benefits: while the latter facilitates visual information in space, the latter is more accurate and considers effects such as the fluctuation of the respiration with time and the interaction between the flow and the person's face.

The two methods are observed to yield similar infection risks, however a larger risk is obtained when considering the average inhalation flow rate. For instance, after 60 s of simulation, the probability based on inhaled particles is 3.5×10^{-8} (Fig. 18, left) which is slightly larger than that near the mouth shown in (Fig. 18, right), where the probability of infections from 5 cm from the mouth of the exposed subject is within 8×10^{-8}-11×10^{-8}.

Thus, even though slightly overestimated, the method based on the average inhalation flow rate gives insightful information on the relation between infection risk and physical-distancing. This is shown in Fig. 18 (right) after 60 s of exposure. At a distance of 30 cm from the mouth, the risk is approximately 5×10^{-7}. Nearer than 30 cm, this risk might increase or decrease depending on the exposed subject's height. At the infected subject's height, the risk increases to about 3×10^{-6} (3 persons in every 1 million). Further than 30 cm from the infected person's mouth the risk decreases logarithmic reaching about 1×10^{-7} (1 in ten million) at 90 cm distance.

The number and mass of droplets inhaled through the nostrils, separated based on particle diameter, are shown in Fig. 20. The numbers of inhaled particles are not integers, because Ansys Fluent represent particles as parcels. Each parcel is weighted by a *strength* number. The number of parcels multiplied by their respective strength equal the actual number of physical particles. The number and mass of inhaled particles peaks at about 30 s from the start of the conversation (close to 30 droplets weighing about 12 ng are inhaled within $t = 25$ s and $t = 30$ s). The majority of inhaled droplets (84%) are of 1 μm diameter (Fig. 20, left), however, droplets of 30 μm amount to 76% of the total mass of inhaled droplets (Fig. 20, right), which is the relevant parameter when estimating the number of virions. Particles smaller than 5 μm (0.8% of the total mass) are negligible for estimating infection risk under the simulated conditions. In addition, during the 60 s of simulation, no parcels deposited on the mouth and only one 30 μm parcel (with a strength number of 0.003) deposited in one of the eyes. This is evidence that the particles were following the flow (aerosols) and being inhaled, rather than simply following semi-ballistic paths and colliding with the subject's face.

The simulation duration of 60 s is sufficient for quantifying the number of droplets inhaled as a result of 15 s of speaking (only 2% of the total mass is inhaled within 50–60 s, Fig. 20, right). Based on the total amount of RNA copies of SARS-CoV-2 inhaled in the first 60 s (0.2313), the probability of infection at longer times is estimated, assuming a reoccurring pattern in the flowing minutes, where the infected person continuously talks during the 15 initial seconds of every minute. The probability of infection based on this extrapolation, obtained from Eq. (15), is shown up to 10 h of conversation in Fig. 21. When considering all exhaled particles (Fig. 21, left), the probability of infection for 1, 3 and 5 h of conversation is, respectively, 2, 6 and 11 persons per million. However, if only small particles (1 and 3 μm) are considered, the probability for the same exposure times reduce to 2, 5 and 8 persons per 100 million. The latter can be considered to be a conservative estimated of infection risk when using masks (particles larger than 5 μm do not penetrate through the mask nor through leakages, see Fig. 9). The actual risk when using masks is expected to be lower, considering the mask penetration (Fig. 9).

7.4. Limitations of this study

Droplet evaporation has been neglected in the case-study presented. Had evaporation been considered (option in the app), the particles would gradually reduce in size and eventually reach their droplet nuclei size. For the initial particle diameters selected this would result in droplet nuclei of 0.25, 0.75, 2.5, 7.5 and 12.5 μm. Additionally, if evaporation had been included, the virion content per

Table 11
DPM boundary conditions.

Boundaries	Droplet behaviour
Nostrils, mouth and walls	Escape
Eyes, other body surfaces and table	Trap

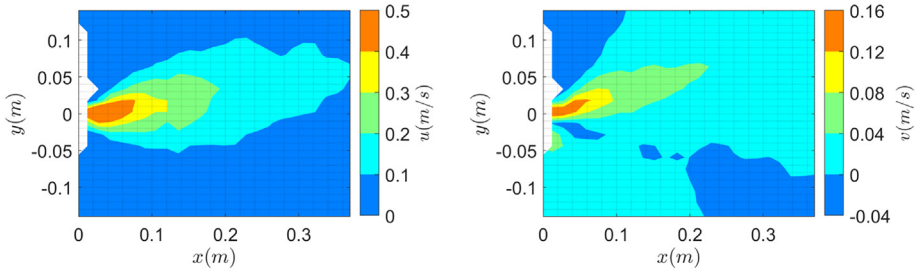

Fig. 16. Average horizontal (left) and vertical (right) velocity during 15 s of simulated speaking (rainbow speech).

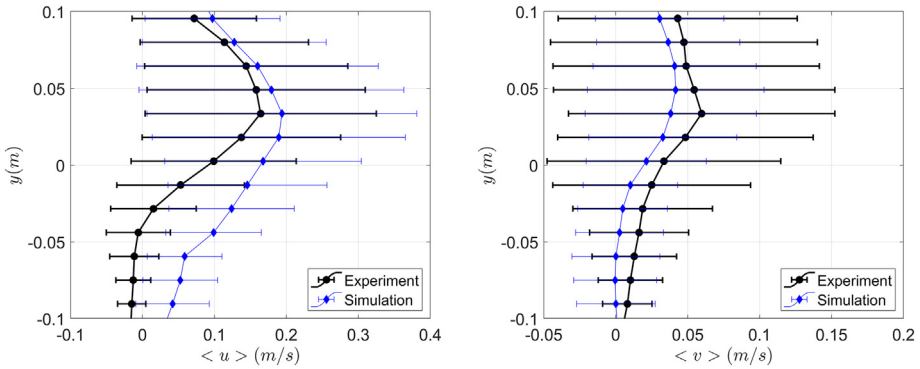

Fig. 17. Comparison of velocity statistics between experiments and simulations at x = 0.2 m. Error bars represent one standard deviation, which is considerably higher for this highly unsteady flow than the PIV measurement uncertainty (order of 1% for the instantaneous velocity, Raffel et al., 2018).

droplet would remain the same (only water evaporates). However, as a droplet reduces from 50 μm to its nucleus size of 12.5 μm, its probability of being inhaled increases. This is seen in Fig. 22, where the fraction of droplets inhaled to droplets deposited on the table is shown to decrease as the particle diameter increases (7.7%, 0.6% and 0.06% for 10, 30 and 50 μm droplets, respectively). Therefore, if evaporation is considered, the number of inhaled droplets of 30 and 50 μm initial diameters would most likely increase considerably, yielding a higher risk of aerosol infection.

8. Summary and conclusions

An application, referred to as *TU Delft COVID-app*, has been developed for a relatively simple and quick CFD simulation setup of human expiratory activities (sneezing, coughing, breathing and speaking) that yield the risk of COVID-19 transmission. The software incorporates data from several experiments from literature and measurements performed in this study. The software also includes probabilistic models to evaluate infection risk probability. The models and data integrated in the tool have been described in detail, laying the foundations of an application that has the potential to democratize the use of CFD for analysis of indoor SARS-CoV-2 spread and associated prevention strategies.

PIV experiments of a person reciting a speech with and without a surgical mask have been performed to obtain the instantaneous air volume flow rate and flow direction at the mouth, allowing for realistic simulations of unsteady speaking. The average flow fields from PIV are compared to that obtained numerically during the simulations. Experimental limitations yielded differences in the average peak velocity of about 20–30% at a distance of 20 cm downstream from the mouth. This is regarded insignificant in comparison to natural biological differences between individuals across the world population.

To demonstrate the capabilities of the application, a numerical simulation of a conversation across a dining/meeting table has been setup in

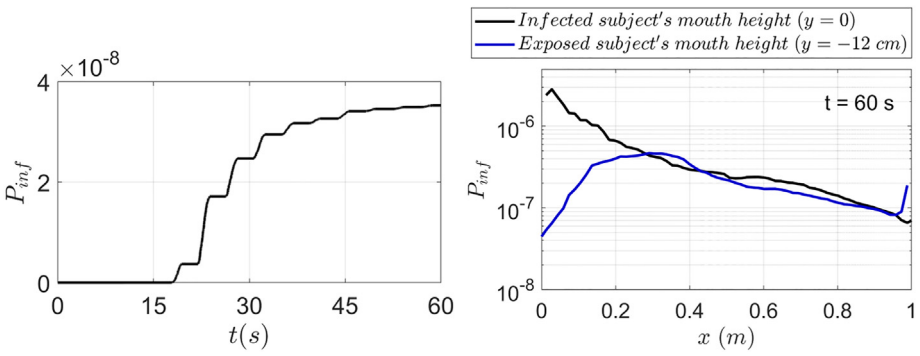

Fig. 18. Left: Probability of infection from inhaled particles vs. time of exposure. Right: Probability of infection based on average inhalation flow rate vs. distance from the mouth after 60 s of exposure.

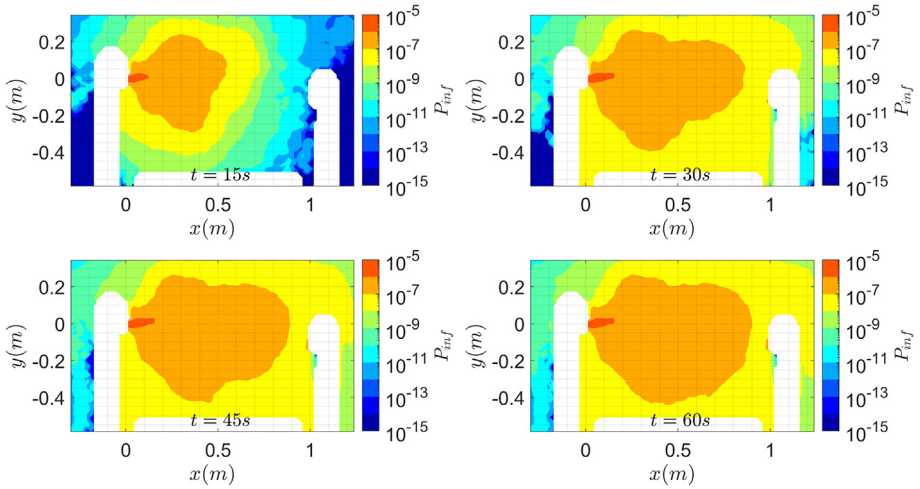

Fig. 19. Probability of infection based on an average inhalation flow rate. In the physical maps of probability of infection, the infected person (male) is on the left and the exposed person (female) is on the right. The probability of infection is cumulative.

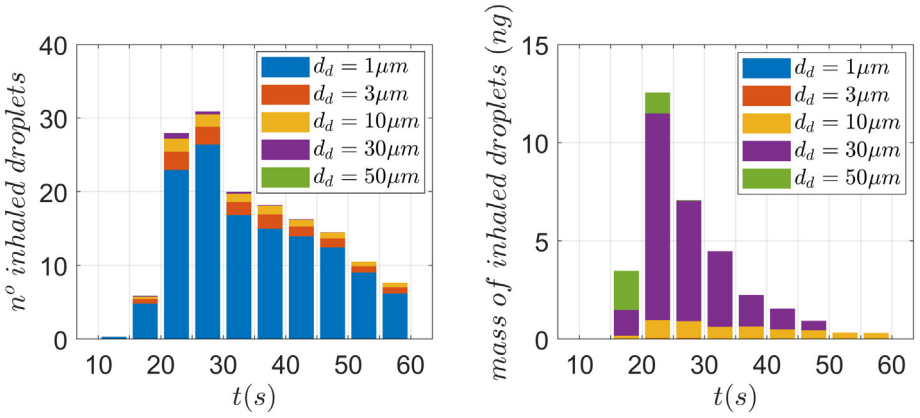

Fig. 20. Number (left) and mass of droplets (right) inhaled during 60 s of simulation.

Ansys Fluent with the TU Delft COVID-app. The simulation results indicate that 1 h of conversation between two persons sitting one-metre apart, where only the infected person talks for one quarter of the time, yields a risk of aerosol infection (droplets <50 μm) of 2 persons per million. However, analysis of the fraction of particles being inhaled as a function of their diameter shows that the estimated risk would be higher had evaporation been considered, as the likelihood of a droplet to be inhaled increases as its diameter reduces as a result of evaporation. When considering only particles smaller than 5 μm (mask penetration diameter threshold) the simulated risk reduces to 2 persons in 100 million, suggesting at least a two orders of magnitude reduction of the risk of infection when face masks are used (the actual mask penetration has not been considered).

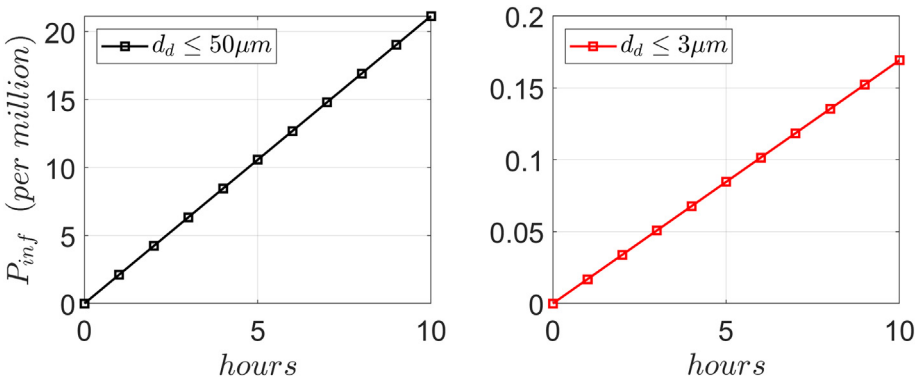

Fig. 21. Long exposure probability of infection. Left: considering all simulated droplets (up to 50 μm). Right: considering only droplets of 1 and 3 μm.

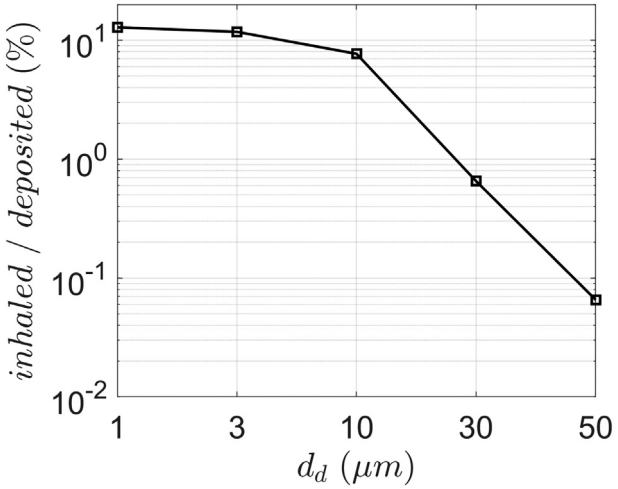

Fig. 22. Fraction of inhaled to deposited (on the table) droplets.

Furthermore, the simulation results show that particles of 10 μm initial diameter or larger are the most relevant when analysing the risk of infection at a one-metre distance conversation.

9. Cautionary note

The TU Delft COVID-app has been developed based on experimental data and an established commercial CFD software (ANSYS Fluent), which yields reliability and accessibility to the application. However, prior to applying the tool for decision making regarding policy measures it is recommended a follow up study that compares results obtained from this application to that of a real life situation. In addition, the results from the case study presented here are mostly illustrative of the application capabilities. It is clear from this analysis that evaporation must be considered in future simulations (readily available at the software).

CRediT authorship contribution statement

David Engler Faleiros: Data curation, Formal analysis, Investigation, Methodology. **Wouter van den Bos:** Conceptualization, Funding acquisition, Project administration, Supervision, Writing – review & editing. **Lorenzo Botto:** Conceptualization, Supervision, Writing – review & editing. **Fulvio Scarano:** Conceptualization, Funding acquisition, Supervision, Writing – review & editing.

Declaration of competing interest

The authors declare that they have no known competing financial interests or personal relationships that could have appeared to influence the work reported in this paper.

Acknowledgements

The authors acknowledge the important contribution of SDC Verifier in translating the application (initially developed in C++) to an integrated software within Ansys Fluent and the TU Delft COVID-19 Response Fund for the financial support. L.B. acknowledges funding from the European Research Council (ERC) under the European Union's Horizon 2020 research and innovation programme (Grant agreement No. 715475).

Appendix A. Cumulative number of SARS-CoV-2 RNA copies inhaled, infectious dose and probability of infection

The cumulative number of RNA copies N, infectious dose ($d = N/16{,}000$) and the probability of infection given by Eq. (15) that have been obtained based on the number of droplets inhaled during the 60 s long simulated conversation (Section 7) and the average viral load in the sputum from Wölfel et al., 2020 (7 billion RNA copies per litre) are given on Table A1.1.

Table A1.1
Cumulative number of SARS-CoV-2 RNA copies, infectious dose and probability of infection based on the number of droplets inhaled during the simulated conversation (Section 7).

t (s)	RNA copies (10^{-2})	Infectious dose (10^{-6})	$\mathbf{P_{inf}}$ (10^{-9})
15	0.0	0.0	0.0
20	2.4	1.5	3.7
25	11.2	7.0	17.1
30	16.2	10.1	24.7
35	19.3	12.1	29.5
40	20.9	13.1	31.9
45	22.0	13.8	33.6
50	22.7	14.2	34.6
55	22.9	14.3	34.9
60	23.1	14.5	35.3

Appendix B. Grid discretization error

The grid discretization error is estimated by calculating changes in the turbulence kinetic energy k in a cross plane, 10 cm downstream from the mouth of the infected person (Fig. A2.1). This process is performed three times, once for the grid used during the simulations of reference size h, followed by two grid refinements by a factor of 2, i.e. for cell sizes of $h/2$ and $h/4$ (the grid itself is non-uniform, but all the cells are scaled accordingly). The simulations are then performed for 1.2 s, where the person starts to speak at 1 s from the start of the simulation. The turbulence kinetic energy is then averaged both in space (along the plane) and time ($t = [1, 1.2]$ s) and compared for different grid sizes (Fig. A2.2).

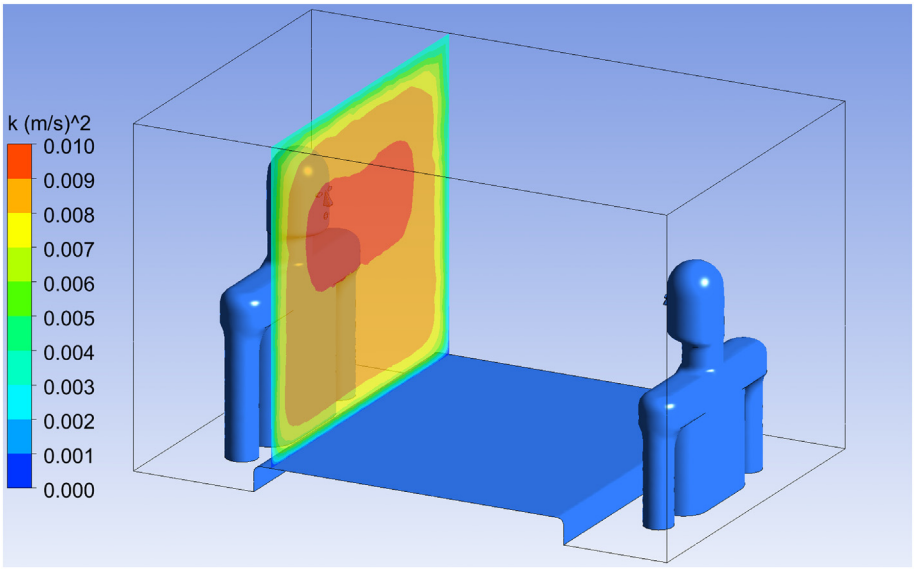

Fig. A2.1. Turbulence kinetic energy in a cross plane 10 cm from the mouth of the infected person.

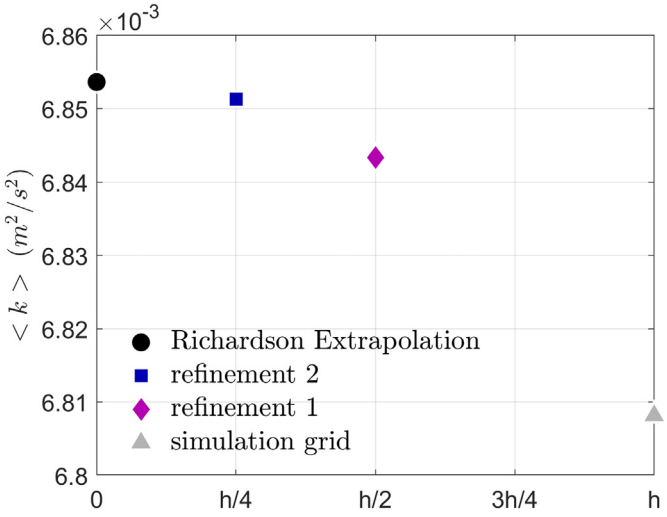

Fig. A2.2. Grid convergence analysis based on averaged turbulence kinetic energy.

The turbulence kinetic energy seems to be converging to a value within [6.85, 6.86] $\times\ 10^{-3}\ \mathrm{m^2/s^2}$. An estimate of k for an infinitesimally small grid cell ($k = 0$) is obtained by using the Richardson extrapolation (Roache, 1998):

$$k_{h=0} = k_{h/4} + \frac{(k_{h/4} - k_{h/2})}{(r^p - 1)}, \tag{A2.1}$$

where $r = 2$ is the grid refinement ratio and p is the order of the grid convergence:

$$p = \ln\left(\frac{k_{h/4} - k_{h/2}}{k_{h/2} - k_h}\right) / \ln(r) \tag{A2.2}$$

The estimated value of $k_{h=0} = 6.8536 \times 10^{-3}\ \mathrm{m^2/s^2}$ (also plotted in Fig. A2.2) is then used as a reference to estimate an error of 0.7% due to grid discretization, in comparison to the value obtained from the grid used during the simulations ($k = 6.8082 \times 10^{-3}\ \mathrm{m^2/s^2}$).

References

Abkarian, M., Mendez, S., Xue, N., Yang, F., Stone, H.A., 2020. Speech can produce jet-like transport relevant to asymptomatic spreading of virus. Proc. Natl. Acad. Sci. U. S. A. 117, 25237–25245.

Alderliesten, M., 2013. Mean particle diameters. Part VII. The rosin-rammler size distribution: physical and mathematical properties and relationships to moment-ratio defined mean particle diameters. Part. Part. Syst. Charact. 30 (244).

Ardon-Dryer, K., Warzywoda, J., Tekin, R., Biros, J., Almodovar, S., Weeks, B.L., Hope-Weeks, L.J., Sacco Jr., A., 2021. Mask material filtration efficiency and mask fitting at the crossroads: implications during pandemic times. Aerosol Air Qual. Res. 21, 200571.

Arumuru, V., Pasa, J., Samantaray, S.S., 2020. Experimental visualization of sneezing and efficacy of face masks and shields. Phys. Fluids 32, 115129.

Asadi, S., Bouvier, N., Wexler, A.S., Ristenpart, W.D., 2020. The coronavirus pandemic and aerosols: does COVID-19 transmit via expiratory particles? Aerosol Sci. Technol. 54, 635.

Bahl, P., de Silva, C., Bhattacharjee, S., Stone, H., Doolan, C., Chughtai, A.A., MacIntyre, C.R., 2021. Droplets and aerosols generated by singing and the risk of coronavirus disease 2019 for choirs. Clin. Infect. Dis. 72, e639.

Bailey, B.J.R., Briars, G.L., 1996. Estimating the surface area of the human body. Stat. Med. 15, 1325.

Bhagat, R.K., Davies Wykes, M.S., Dalziel, S.B., Linden, P.F., 2020. Effects of ventilation on the indoor spread of COVID-19. J. Fluid Mech. 903, F1.

Bhattacharyya, S., Dey, K., Paul, A.R., Biswas, R., 2020. A novel CFD analysis to minimize the spread of COVID-19 virus in hospital isolation room. Chaos Solit Fractals 139, 110294.

Bluyssen, P.M., Ortiz, M., Zhang, D., 2021. The effect of a mobile HEPA filter system on 'infectious' aerosols, sound and air velocity in the SenseLab. Build. Environ. 188, 107475.

Bourouiba, L., 2020. Turbulent gas clouds and respiratory pathogen emissions: potential implications for reducing transmission of COVID-19. JAMA 323, 1837.

Bourouiba, L., Dehandschoewercker, E., Bush, J., 2014. Violent expiratory events: on coughing and sneezing. JFM 745, 537.

Brlek, A., Vidovič, Š., Vuzem, S., Turk, K., Simonović, Z., 2020. Possible indirect transmission of COVID-19 at a squash court, Slovenia, march 2020: case report. Epidemiol. Infect. 148, e120.

Busco, G., Yang, S.R., Seo, J., Hassan, Y.A., 2020. Sneezing and asymptomatic virus transmission. Phys. Fluids 32, 073309.

Chao, C.Y.H., Wan, M.P., Morawska, L., Johnson, G.R., Ristovski, Z.D., Hargreaves, M., Mengersen, K., Corbett, S., Li, Y., Xie, X., Katoshevski, D., 2009. Characterization of expiration air jets and droplet size distributions immediately at the mouth opening. J. Aerosol Sci. 40, 122.

Cho, K.J., Mckay, T.R.R., Shukla, R., Haruta, H., Sekar, P., Grinshpun, S.A., 2010. Large particle penetration through N95 respirator filters and facepiece leaks with cyclic flow. Ann. Occup. Hyg. 54, 68.

Cortellessa, G., Stabile, L., Arpino, F., Faleiros, D.E., van den Bos, W., Morawska, L., Buonanno, G., 2021. Close proximity risk assessment for SARS-CoV-2 infection. Sci. Total Environ. 794, 148749.

Duguid, J.P., 1946. The size and the duration of air-carriage of respiratory droplets and droplet-nuclei. Epidemiol. Infect. 44, 471.

Fairbanks, G., 1960. Voice and Articulation Drillbook, 2nd edn. Harper & Row, New York, pp. 124–139.

Goldman, E., 2020. Exaggerated risk of transmission of COVID-19 by fomites. Lancet Infect. Dis. 20, 892. published online July 3.

Gregson, F.K.A., Watson, N.A., Orton, C.M., Haddrell, A.E., McCarthy, L.P., Finnie, T.J.R., Gent, N., Donaldson, G.C., Shah, P.L., Calder, J.D., Bzdek, B.R., Costello, D., Reid, J.P., 2021. Comparing aerosol concentrations and particle size distributions generated by singing, speaking and breathing. Aerosol Sci. Technol. 55, 681.

Grinshpun, S.A., Haruta, H., Eninger, R.M., Reponen, T., McKay, R.T., Lee, S.-A., 2009. Performance of an N95 filtering facepiece particulate respirator and a surgical mask during human breathing: two pathways for particle penetration. J. Occup. Environ. Hyg. 6, 593.

Gupta, J.K., Lin, C.-H., Chen, Q., 2009. Flow dynamics and characterization of a cough: flow dynamics and characterization of a cough. Indoor Air 19, 517.

Gupta, J.K., Lin, C.-H., Chen, Q., 2010. Characterizing exhaled airflow from breathing and talking. Indoor Air 20, 31.

Gupta, J.K., Lin, C.-H., Chen, Q., 2011. Transport of expiratory droplets in an aircraft cabin: transport of expiratory droplets in an aircraft cabin. Indoor Air 21, 3.

Kähler, C.J., Hain, R., 2020. Fundamental protective mechanisms of face masks against droplet infections. J. Aerosol Sci. 148, 105617.

Khosronejad, A., Santoni, C., Flora, K., Zhang, Z., Kang, S., Payabvash, S., Sotiropoulos, F., 2020. Fluid dynamics simulations show that facial masks can suppress the spread of COVID-19 in indoor environments. AIP Adv. 10, 125109.

Kitazawa, K., Deinhardt-Emmer, S., Inomata, T., Deshpande, S., Sotozono, C., 2021. The transmission of SARS-CoV-2 infection on the ocular surface and prevention strategies. Cells 10, 796.

Klompas, M., Baker, M.A., Rhee, C., 2020. Airborne transmission of SARS-CoV-2: theoretical considerations and available evidence. JAMA 324, 441.

Lee, B.U., Yermakov, M., Grinshpun, S.A., 2005. Filtering efficiency of N95- and R95-type facepiece respirators, dust-mist facepiece respirators, and surgical masks operating in unipolarly ionized indoor air environments. Aerosol Air Qual. Res. 5, 25.

Lelieveld, J., Helleis, F., Borrmann, S., Cheng, Y., Drewnick, F., Haug, G., Klimach, T., Sciare, J., Su, H., Pöschl, U., 2020. Model calculations of aerosol transmission and infection risk of COVID-19 in indoor environments. IJERPH 17, 8114.

Li, Y., Qian, H., Hang, J., Chen, X., Cheng, P., Ling, H., Wang, S., Liang, P., Li, J., Xiao, S., Wei, J., Liu, L., Cowling, B.J., Kang, M., 2021. Probable airborne transmission of SARS-CoV-2 in a poorly ventilated restaurant. Build. Environ. 196, 107788.

Liu, L., Wei, J., Li, Y., Ooi, A., 2017. Evaporation and dispersion of respiratory droplets from coughing. Indoor Air 27, 179.

Mansour, E., Vishinkin, R., Rihet, S., Saliba, W., Fish, F., Sarfati, P., Haick, H., 2020. Measurement of temperature and relative humidity in exhaled breath. Sens Actuators B Chem 304, 127371.

Mei, R., 1996. Velocity fidelity of flow tracer particles. Exp. Fluids 22, 1.

Menter, F.R., Kuntz, M., Langstry, R., 2003. Ten years of industrial experience with the SST turbulence model. Turbulence, Heat and Mass Transfer. 4, p. 625.

Metzmacher, H., Wölki, D., Schmidt, C., Frisch, J., van Treeck, C., 2018. Real-time human skin temperature analysis using thermal image recognition for thermal comfort assessment. Energ Build. 158, 1063.

Meyerowitz, E.A., Richterman, A., Gandhi, R.T., Sax, P.E., 2021. Transmission of SARS-CoV-2: a review of viral, host, and environmental factors. Ann. Intern. Med. 174, 69.

Mittal, R., Ni, R., Seo, J.-H., 2020. The flow physics of COVID-19. J. Fluid Mech. 894, F2.

Morris, D.H., Yinda, K.C., Gamble, A., Rossine, F.W., Huang, Q., Bushmaker, T., Fischer, R.J., Matson, M.J., Van Doremalen, N., Vikesland, P.J., Marr, L.C., Munster, V.J., Lloyd-Smith, J.O., 2021. Mechanistic theory predicts the effects of temperature and humidity on inactivation of SARS-CoV-2 and other enveloped viruses. eLife 10, e65902.

Morsi, S.A., Alexander, A.J., 1972. An investigation of particle trajectories in two-phase flow systems. J. Fluid Mech. 55, 193.

Prather, K.A., Marr, L.C., Schooley, R.T., McDiarmid, M.A., Wilson, M.E., Milton, D.K., 2020. Airborne transmission of SARS-CoV-2. Science https://doi.org/10.1126/science.abf0521.

Qian, Y., Willeke, K., Grinshpun, S.A., Donnelly, J., Coffey, C.C., 1998. Performance of N95 respirators: filtration efficiency for airborne microbial and inert particles. Am. Ind. Hyg. Assoc. J. 59, 128.

Raffel, M., Willert, C.E., Scarano, F., Kähler, C., Wereley, S.T., Kompenhans, J., 2018. Particle Image Velocimetry. A Practical Guide. 3rd ed. Springer International Publishing.

Ren, J., Wang, Y., Liu, Q., Liu, Y., 2021. Numerical study of three ventilation strategies in a prefabricated COVID-19 inpatient ward. Build. Environ. 188, 107467.

Roache, P.J., 1998. Verification and Validation in Computational Science and Engineering. Hermosa Publishers, Albuquerque, New Mexico.

Rodriguez-Martinez, A., et al., 2020. Height and body-mass index trajectories of school-aged children and adolescents from 1985 to 2019 in 200 countries and territories: a pooled analysis of 2181 population-based studies with 65 million participants. Lancet 396, 1511.

Sender, R., Bar-On, Y.M., Gleizer, S., Bernsthein, B., Phillips, R., Milo, R., 2021. The total number and mass of SARS-CoV-2 virions. PNAS 118, 25.

Shen, Y., Li, C., Dong, H., Wang, Martinez, L., Sun, Z., Handel, A., Chen, Z., Chen, E., Ebell, M.H., Wang, F., Yi, B., Wang, H., Wang, X., Wang, A., Chen, B., Qi, Y., Liang, L., Li, Y., Ling, F., Chen, J., Xu, G., 2020. Community outbreak investigation of SARS-CoV-2 transmission among bus riders in eastern China. JAMA Intern Med 180, 1665.

Staymates, M., 2020. Flow visualization of an N95 respirator with and without an exhalation valve using Schlieren imaging and light scattering. Phys. Fluids 32, 111703.

Sun, S., Li, J., Han, J., 2021. How human thermal plume influences near-human transport of respiratory droplets and airborne particles: a review. Environ. Chem. Lett. 19, 1971.

Tang, J.W., Liebner, T.J., Craven, B.A., Settles, G.S., 2009. A Schlieren optical study of the human cough with and without wearing masks for aerosol infection control. J. R. Soc. Interface 6.

TU Delft, 2021. COVID-app. https://sdcverifier.com/software/tu-delft-covid-app/.

Van Doremalen, N., Bushmaker, T., Morris, D.H., Holbrook, M.G., Gamble, A., Williamson, B.N., Tamin, A., Harcourt, J.L., Thornburg, N.J., Gerber, S.I., Lloyd-Smith, J.O., de Wit, E., Munster, V.J., 2020. Aerosol and surface stability of SARS-CoV-2 as compared with SARS-CoV-1. N. Engl. J. Med. 382, 1564.

Verma, S., Dhanak, M., Frankenfield, J., 2020. Visualizing the effectiveness of face masks in obstructing respiratory jets. Phys. Fluids 32, 061708.

Vesilind, P.A., 1980. The rosin-rammler particle size distribution. Resour. Recov. Conserv. 5, 275.

Watanabe, T., Bartrand, T.A., Weir, M.H., Omura, T., Haas, C.N., 2010. Development of a dose-response model for SARS coronavirus: dose-response model for SARS-CoV. Risk Anal. 30, 1129.

Wells, W.F., 1934. On air-borne infection. Study II. Droplets and droplet nuclei. Am. J. Hyg. 20, 611.

WHO, 2014. Infection Prevention and Control of Epidemic-and Pandemic-Prone Acute Respiratory Infections in Health Care. WHO Guidelines. World Health Organization.

Wölfel, R., Corman, V.M., Guggemos, W., Seilmaier, M., Zange, S., Müller, M.A., Niemeyer, D., Jones, T.C., Vollmar, P., Rothe, C., Hoelscher, M., Bleicker, T., Brünink, S., Schneider, J., Ehmann, R., Zwirglmaier, K., Drosten, C., Wendtner, C., 2020. Virological assessment of hospitalized patients with COVID-2019. Nature 581, 465.

Xie, X., Li, Y., Chwang, A.T.Y., Ho, P.L., Seto, W.H., 2007. How far droplets can move in indoor environments – revisiting the Wells evaporation-falling curve. Indoor Air 17, 211.

Xie, X., Li, Y., Sun, H., Liu, L., 2009. Exhaled droplets due to talking and coughing. J. R. Soc. Interface 6, S703–S714.

Zhang, R., Li, Y., Zhang, A.L., Wang, Y., Molina, M.J., 2020. Identifying airborne transmission as the dominant route for the spread of COVID-19. Proc. Natl. Acad. Sci. U. S. A. 117, 14857.

Zhu, S., Kato, S., Yang, J.-H., 2006. Study on transport characteristics of saliva droplets produced by coughing in a calm indoor environment. Build. Environ. 41, 1691.